

Design of High-Performance Pyridine/Quinoline Hydrazone Photoswitches

Bernard Mravec, Šimon Budzák,* Miroslav Medved', Lukáš F. Pašteka, Chavdar Slavov, Torben Saßmannshausen, Josef Wachtveitl, Jozef Kožíšek, Lea Hegedüsová, Juraj Filo, and Marek Cigán*



Cite This: <https://doi.org/10.1021/acs.joc.1c01174>



Read Online

ACCESS |



Metrics & More

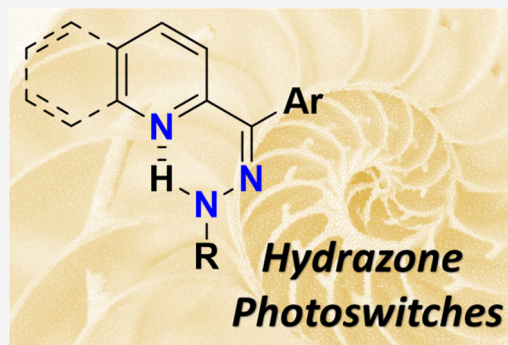


Article Recommendations



Supporting Information

ABSTRACT: The design of P-type photoswitches with thermal stability of the metastable form of hundreds of years that would efficiently transform using excitation wavelengths above 350 nm remains a challenge in the field of photochromism. In this regard, we designed and synthesized an extended set of 13 pyridine/quinoline hydrazones and systematically investigated the structure–property relationships, defining their kinetic and photoswitching parameters. We show that the operational wavelengths of the pyridine hydrazone structural motif can be effectively shifted toward the visible region without simultaneous loss of their high thermal stability. Furthermore, we characterized the ground-state and excited-state potential energy surfaces with quantum-chemical calculations and ultrafast transient absorption spectroscopy, which allowed us to rationalize both the thermal and photochemical reaction mechanisms of the designed hydrazones. Whereas introducing an electron-withdrawing pyridyl moiety in benzoylpyridine hydrazones leads to thermal stabilities exceeding 200 years, extended π -conjugation in naphthoquinoline hydrazones pushes the absorption maxima toward the visible spectral region. In either case, the compounds retain highly efficient photoswitching characteristics. Our findings open a route to the rational design of a new family of hydrazone-based P-type photoswitches with high application potential in photonics or photopharmacology.



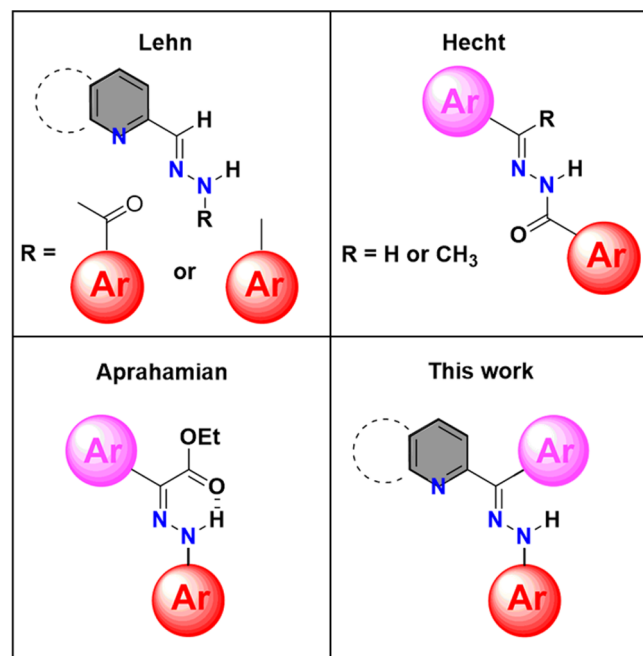
INTRODUCTION

P-type photochromic compounds with the high thermal stability of the thermodynamically less stable form have received increasing attention from the scientific community as they can be used as light-controlled molecular switches in a wide range of applications in opto-(bio)electronics^{1–7} and photopharmacology,^{8–12} including 3D visualization in volumetric displays¹³ and precise temporal and spatial control over drug delivery.¹⁴ In recent years, Hecht¹⁵ and Fuchter¹⁶ showed that the thermal isomerization half-lives of azoarenes, the most widely used configurational photoswitches, can be increased up to 2–3 years by functionalization of an azobenzene skeleton with *o*-fluorine substituents or with an appropriate methyl substitution pattern on arylazopyrazoles. A breakthrough in this direction was achieved by Aprahamian and his co-workers, who discovered that a new family of configurational P-type photoswitches based on a hydrazone skeleton exhibits extraordinary half-lives of hundreds up to thousands of years.^{17,18} Contrary to parent photochemically locked *E*- and *Z*-isomers of pyridine hydrazones/acylhydrazones introduced by Aprahamian¹⁹ and Lehn,²⁰ respectively, the replacement of a pyridyl ring by a phenyl in Aprahamian's ketoester hydrazones led to excellent bistable photoswitching (Scheme 1). However, recent efforts to induce a red shift of the absorption maxima of the core ketoester hydrazone structural

motif by planarization of the structure resulted in an undesired decrease in the photoswitch thermal stability (from hundreds of years to approximately 20 days).²¹ Earlier, Hecht's group also prepared several P-type acylhydrazone photoswitches containing pyridine subunit, although without quantitative determination of the thermal half-lives.²² Although excellent improvement in the absorption red shift of azoarenes as configurational photoswitches to vis/NIR region has been achieved by research groups of Herges and Woolley, their half-lives usually do not exceed several hours or days.^{23–28} To the best of our knowledge, the only exception is the DOM-azo dye stable for months in neutral aqueous solutions.²⁸ Very recently, we proposed an alternative structural modification leading to 2-(benzoyl)pyridine hydrazone photochromes (including compound 1 in Scheme 1) which mimic the photoswitching characteristics of ketoester hydrazones exhibiting relatively good thermal stability (up to 1.9 years) and absorption in the UV region.^{29,30} We showed that introducing an electron-

Received: May 20, 2021

Scheme 1



withdrawing (EW) *p*-nitro group on the ketone phenyl ring of 2-(benzoyl)pyridine hydrazones leads to a significant improvement of the photoswitch addressability, fatigue resistance, and also mutual ratio of *Z*-to-*E* and *E*-to-*Z* photoisomerization efficiency compared to an electron-donating (ED) *p*-dimethylamino substituent.²⁹

Here, we present 12 newly synthesized 2-(*p*-nitrobenzoyl)pyridine/2-(*p*-cyanobenzoyl)pyridine/2-(naphthoyl)quinoline hydrazone photoswitches (Scheme 2; SI, the Synthesis section) designed to gain insight into the photoswitching mechanism and reveal the underlying structure–property relationships for this type of chromophores. To study these relationships in detail, we employed both quantum-chemical calculations and photochemical experiments including ultrafast transient absorption spectroscopy. We show that extended π -conjugation of the parent 2-(benzoyl)pyridine structural motif by fused aromatic rings shifts the photoswitching to desired longer wavelengths with sufficient thermal stability of several years. A detailed understanding of the topology of the ground-state (GS) and excited-state (ES) potential energy surfaces (PES) opens a route to the design of new hydrazone-based P-type photoswitches, with high application potential in both optoelectronics and photopharmacology.

RESULTS AND DISCUSSION

We designed a group of eight 2-(*p*-nitrobenzoyl)pyridine hydrazones 1–8 (Scheme 1) to investigate the substitutional effects on the hydrazine ring on the thermal stability and the photophysical characteristics of hydrazones. In addition, to corroborate the role of an EW substituent in the *para* position of the ketone phenyl ring, cyano derivatives 9 and 10 were also synthesized and thoroughly characterized. Finally, three 2-(naphthoyl)quinoline hydrazones 11–13 were designed to pursue the possibility of shifting the photoactivity of the photochromes to longer wavelengths.

For the sake of consistency with the mechanism (*vide infra*), we will use terms “ketone” and “hydrazine” parts to refer to the upper and lower moieties, respectively, of the skeleton

displayed in Scheme 2 instead of “rotor” and “stator” used in previously published articles related to hydrazone photoswitches, because the rotation of the N–N bond in the “stator” part plays a key role in both the thermal and photochemical isomerization of the studied hydrazones.

Thermal *E*-to-*Z* Isomerization. Aprahamian’s research group showed that EW groups (–CN, –NO₂) in the *para* position of the hydrazine phenyl ring of ketoester hydrazones resulted in a 3–4 fold increase in thermal stability, whereas ED groups (–OCH₃, –NMe₂) led to a rather unexpected 6 orders of magnitude decrease in thermal half-lives.¹⁸ They hypothesized that the acceleration of the *E*-to-*Z* thermal isomerization results from the partial single-bond character of the C=N double bond due to the mesomeric (+M) effect of the ED substituents changing the reaction mechanism from inversion to rotation. However, only a qualitative explanation was provided. The substitutional effect in the ketone part of the molecule was found to be less pronounced.^{18,29} Although a system with the ketone part containing an electron-donating –NMe₂ group proved to be thermally more stable compared to that with electron-withdrawing –NO₂, the difference in thermal stability was rather small. The set of 13 hydrazones presented in this work enables us to study the structure–thermal stability relationships in detail.

To quantify the effect of the electronic changes induced by a hydrazine aromatic ring in the 2-(*p*-nitrobenzoyl)pyridine hydrazones 1–7, we constructed a Hammett plot³¹ using σ_p^- values³² that describe the stabilization of negative charge through resonance (Figure 1; SI, Table S1). The rate of the thermal back isomerization represented by the corresponding rate constant k_x decreases with the increasing σ_p^- value (exception being the pentafluorophenyl substituent), in line with the previous study.¹⁸ However, contrary to ketoester hydrazones, the presence of a strong ED methoxy substituent does not lead to the acceleration of the *E*-to-*Z* thermal isomerization and thus to the hypothesized change of the reaction mechanism from inversion to rotation of the imine bond. The deviation of –C₆F₅ from the otherwise strongly linear dependence can be explained by a decreased level of conjugation with the hydrazine moiety caused by the partial rotation of the aryl ring ($\sim 20^\circ$) due to the steric repulsion between the *o*-F and N lone pairs. Excluding the –C₆F₅ derivative from the analysis significantly improves the correlation, thus enabling a confident prediction of the thermal stability simply based on the σ_p^- values. Let us note that the traditional Swain–Lupton analysis^{31–34} distinguishing between the influence of inductive and mesomeric/resonance effects of the hydrazine ring on the rate of the thermal isomerization is not applicable in the present study (see discussion in the SI).

Our quantum-chemical calculations at the ω B97XD/def2-TZVPP level³⁵ revealed a rather complex three-step inversion-rotation reaction mechanism of the thermal *E*-to-*Z* isomerization of 2-(*p*-nitrobenzoyl)pyridine hydrazones. The reaction path can be illustrated using molecule 7 as an example (Figure 2). The initial step is the C=N bond inversion which is also the rate-limiting step with the calculated activation energy equal to 31.2 kcal/mol. The relaxation proceeds to a shallow local minimum L₁. Here, the energetically less expensive N–N single bond rotation occurs with the barrier of 3.0 kcal/mol, bringing the system to a fleeting local minimum L₂. The last step toward the global *Z* minimum requires a low-energy rotation (barrier 0.1 kcal/mol) of the ketone pyridyl ring, establishing an optimal configuration with a hydrogen bond.

Scheme 2

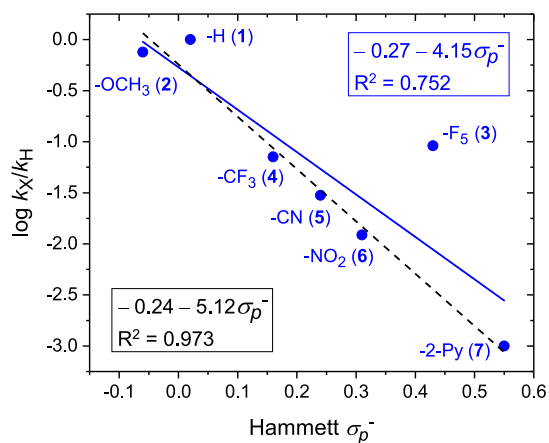
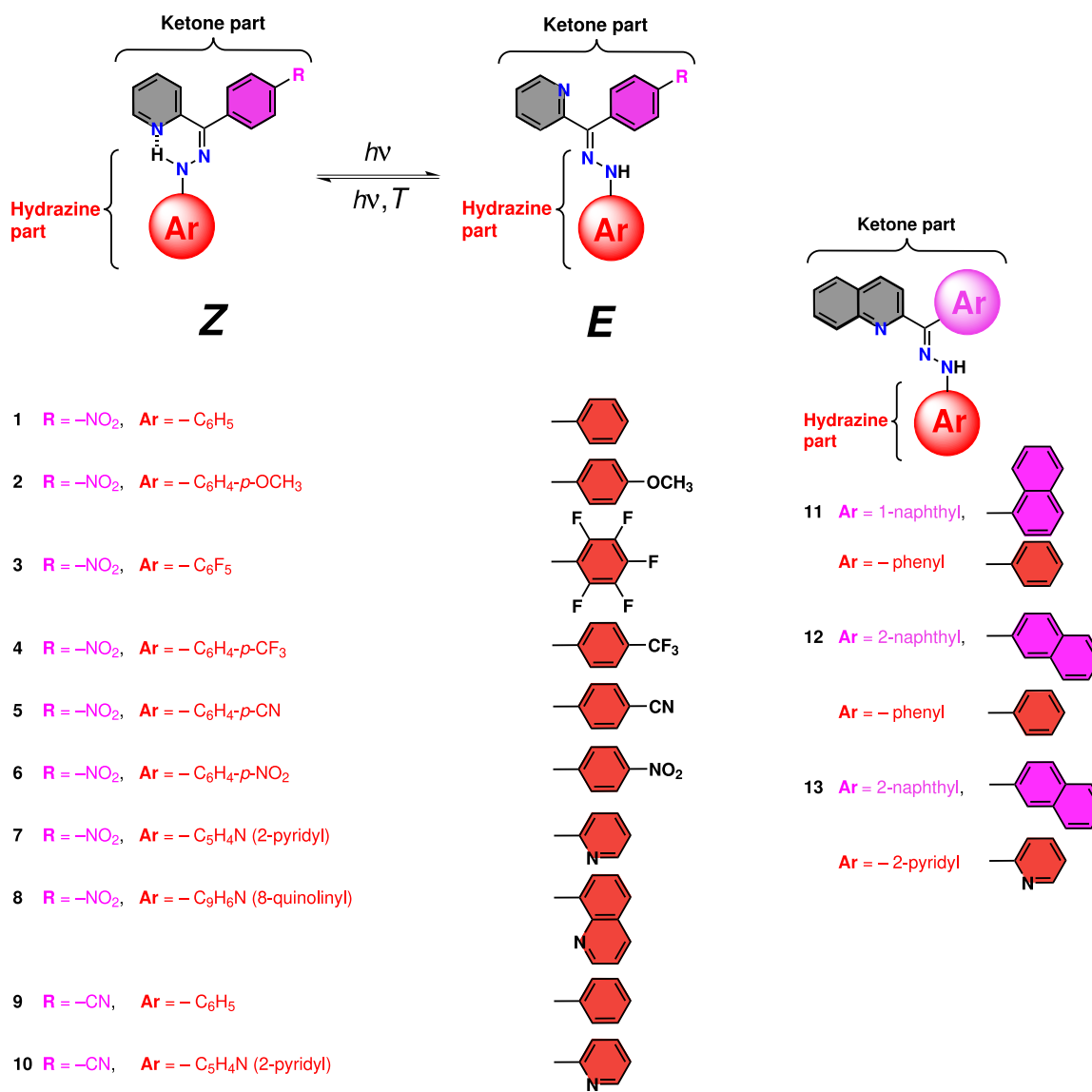


Figure 1. Hammett plot; σ_p^- , Hammett constant; k_X , rate constant of *E*-to-*Z* thermal isomerization of hydrazones 1–7 with substituent X; k_H , rate constant of *E*-to-*Z* thermal isomerization of hydrazone 1. The solid line represents a linear fit through all points; the dashed line represents a linear fit excluding the -F₅ outlier.

The experimentally determined Gibbs activation energy values of the *E*-to-*Z* thermal isomerization (Table 1) agree well with the calculated overall ΔG^\ddagger values for the representative hydrazones 1 and 7 (SI, Table S2). The negative slope (sensitivity constant) of the Hammett plot in Figure 1 indicates that the reduced electron density on the hydrazone NH nitrogen by the EW hydrazine aromatic ring hinders the sp^2/sp rehybridization of the neighboring hydrazone C=N nitrogen in the inversion transition state (TS) (Figure 3). The molecular orbital (MO) analysis revealed that the activation barrier of inversion is indeed predominantly related to an increase of the orbital energy of the nitrogen lone pair (Figure 3B) by 42.8 and 43.5 kcal/mol for 1 and 7, respectively, which is partially balanced by the stabilization of the highest occupied MO (HOMO) (delocalized π -orbital) by -5.8 and -5.0 kcal/mol, respectively (SI, Table S3 and Figure S104). Interestingly, the EW character of the hydrazine moiety of 7 stabilizes the lone pair orbital as well as the HOMO in both the *E* isomer and the TS. However, the stabilization is more pronounced in the *E* minimum, which results in a higher activation barrier for

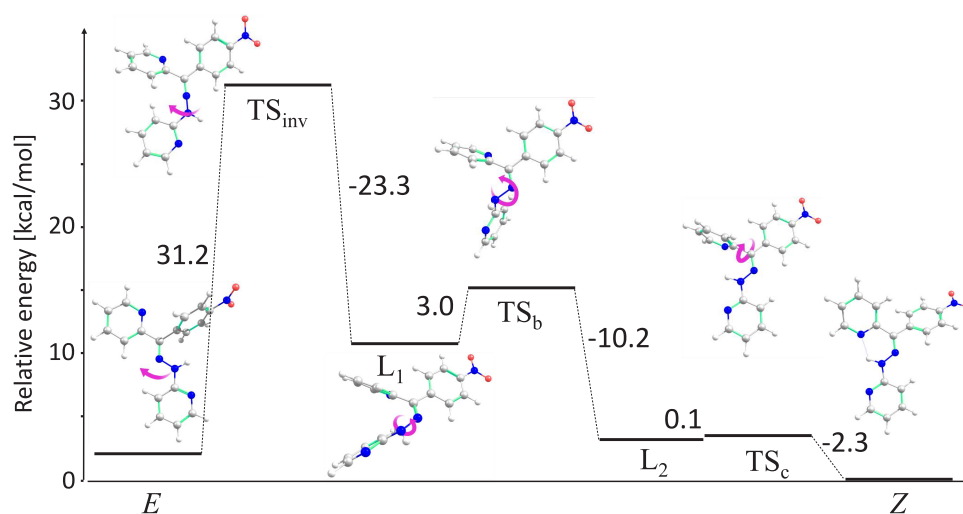


Figure 2. Reaction path profile for thermal *E*-to-*Z* transformation of hydrazone **7** calculated at ω B97XD/def2-TZVP level of theory (see Video S2).

Table 1. Kinetic Data and Activation Parameters for the *E*-to-*Z* Thermal Isomerization of the Studied Hydrazone *E*-Isomers in Toluene- d_8 ($T = 298.15$ K; Determined from ^1H NMR Experimental Data)

hydrazone	k^a [s^{-1}]	$\tau_{1/2}^b$ [year]	E_a^c [kcal/mol]	$\Delta H^{\ddagger d}$ [kcal/mol]	$\Delta S^{\ddagger d}$ [cal/(mol K)]	$\Delta G^{\ddagger d}$ [kcal/mol]
(<i>E</i>)-1	$1.09(31) \times 10^{-7}$	0.20(11)	27.64(15)	26.65(15)	-0.43(40)	26.95(15)
(<i>E</i>)-2	$8.21(110) \times 10^{-8}$	0.26(5)	27.82(7)	27.12(9)	-0.03(0)	27.12(9)
(<i>E</i>)-3	$9.95(49) \times 10^{-9}$	2.21(12)	29.07(14)	28.37(3)	0.23(1)	28.37(3)
(<i>E</i>)-4	$7.73(20) \times 10^{-9}$	2.84(43)	29.22(4)	28.52(9)	0.10(14)	28.52(9)
(<i>E</i>)-5	$3.26(75) \times 10^{-9}$	6.72(39)	29.72(12)	29.03(18)	-0.10(58)	29.03(18)
(<i>E</i>)-6	$1.33(36) \times 10^{-9}$	16.4(62)	30.25(55)	29.56(19)	-0.01(37)	29.56(19)
(<i>E</i>)-7	$1.09(22) \times 10^{-10}$	200(50)	31.73(13)	31.04(13)	-0.16(3)	31.04(13)
(<i>E</i>)-8	$7.78(84) \times 10^{-10}$	28.2(35)	30.57(9)	30.03(16)	0.15(8)	29.88(7)
(<i>E</i>)-9	$2.48(61) \times 10^{-8}$	0.89(29)	28.52(21)	27.83(24)	0.31(7)	27.83(24)
(<i>E</i>)-10	$7.97(168) \times 10^{-11}$	280(70)	31.92(18)	31.23(14)	-0.06(4)	31.23(14)
(<i>E</i>)-11	$1.18(36) \times 10^{-7}$	0.17(9)	27.70(19)	26.90(11)	-0.08(4)	26.90(11)
(<i>E</i>)-12	$3.38(62) \times 10^{-9}$	6.50(142)	29.71(15)	29.01(12)	0.37(5)	29.01(12)
(<i>E</i>)-13	$5.95(34) \times 10^{-8}$	0.37(2)	28.00(23)	27.31(4)	0.17(3)	27.31(4)

^aRate constant of *E*-to-*Z* isomerization determined by nonlinear fitting of experimental data (including back thermal *Z*-to-*E* isomerization).

^bThermal stability of the thermodynamically less stable *E*-isomer (calculated from the experimentally determined rate constant k). ^cActivation barrier calculated using the Arrhenius equation. ^dThermodynamic activation parameters calculated using the Eyring equation.

the inversion and thus also higher thermal stability of **7** compared to **1**.

The rotation as a possible pathway can be clearly ruled out since the calculated activation energy is 12.4 and 12.3 kcal/mol higher compared to inversion for hydrazones **1** and **7**, respectively (SI, Table S2). Note that the calculated activation entropy for inversion and rotation has practically the same value (SI, Table S2); therefore, the activation entropy cannot be used to experimentally distinguish between the inversion and rotation mechanisms of the thermal isomerization of hydrazones.

Kinetic data (rate constants and thermal half-lives) and other activation parameters for the studied hydrazones are summarized in Table 1. Unambiguously, the half-life of the *E*-to-*Z* thermal isomerization increases with increasing EW character of the hydrazine ring (consider hydrazones **1**–**8**). The hydrazone photoswitch **7** with the pyridyl hydrazine ring achieves an excellent thermal stability of 200 years. Due to the number of commercially available 2-pyridyl hydrazines, this skeleton could be further modified to immobilize the

photoswitch onto various surfaces or incorporate the photoswitch into a biomolecule. Moreover, contrary to a more than 50-fold decrease in thermal stability of the parent hydrazone **1** in polar solvents,²⁹ hydrazone **7** retains good thermal stability also in a polar environment (~ 35 years in acetonitrile- d_3).

To demonstrate the effect of the 2-pyridyl hydrazine ring on the thermal stability of benzoylpyridine hydrazones with *p*-acceptor substituted ketone phenyl ring, we designed cyano derivatives **9** and **10** (Scheme 2; Table 1). The incorporation of the 2-pyridyl hydrazine ring instead of the phenyl leads to a significant increase in the photoswitch thermal stability from 0.9 to 280 years in line with our previous findings on the related hydrazones **1** and **7**. However, in the case of the 2-(naphthoyl)quinoline hydrazone **13**, the analogous substitution unexpectedly reduces the thermal stability as compared to the parent hydrazone **12**, which exhibits a remarkable half-life of 6.5 years, indicating that the electron distribution in the thermally active central hydrazone skeleton of **13** linked to a weak acceptor (quinoline), a stronger acceptor (2-pyridyl), and

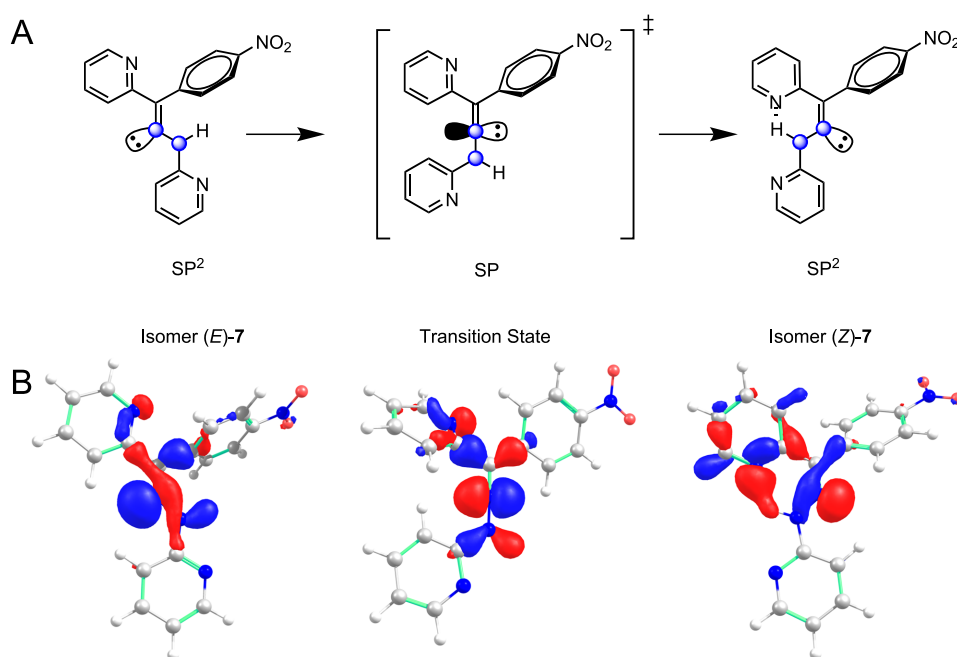


Figure 3. (A) The sp^2/sp rehybridization of hydrazone C=N nitrogen in the inversion transition state of *E*-to-*Z* thermal isomerization of studied 2-(*p*-nitrobenzoyl)pyridine hydrazones. (B) Change of lone pair orbital during the *E*-to-*Z* inversion reaction. The isosurface value is 0.05.

Table 2. Photoswitching Parameters of Hydrazones 1–13 Measured in Toluene ($T = 298.15$ K)^a

hydrazone	ϵ/λ_{\max}		Φ		PSS (<i>E</i> / <i>Z</i>)	
	<i>E</i>	<i>Z</i>	<i>E</i> → <i>Z</i>	<i>Z</i> → <i>E</i>	<i>E</i> → <i>Z</i>	<i>Z</i> → <i>E</i>
1	21200/338/	18700/406/	1.9(2)	0.3(1)	13:87	80:20
2	11000/351/	12000/423/	1.2(2)	0.4(1)	16:84	69:31
3	26400/310/	22400/367/	12.3(21)	0.8(3)	4:96	49:51
4	18400/332/	18500/394/	8.7(11)	0.8(3)	2:98	67:33
5	21300/341/	23900/400/	9.1(11)	1.4(1)	5:95	50:50
6	23900/388/	27500/417/	1.6(5)	0.01(3)	1:99	7:93
7	28400/322/	31000/387/	8.4(11)	1.9(4)	15:85	83:17
8	22000/384/	22100/429/	0.3(1)	0.05(1)	2:98	65:35
9	20400/353/	25700/391/	1.3(2)	0.4(1)	18:82	75:25
10	25600/338/	28400/373/	3.6(4)	0.13(3)	5:95	63:37
11	27100/369/	13200/427/	1.8(2)	2.0(2)	25:75	96:4
12	36000/370/	20600/432/	6.8(4)	2.1(2)	5:95	93:7
13	39000/361/	20600/407/	8.4(6)	1.1(4)	7:93	83:17

^a ϵ , molar absorption (extinction) coefficient (in $\text{dm}^3 \text{mol}^{-1} \text{cm}^{-1}$); λ_{\max} , UV–vis absorption maximum (in nm); Φ , quantum yield of photoisomerization (in %); PSS, photostationary state composition at the corresponding irradiation wavelength (in %; irradiation wavelength: PSS (*E* → *Z*): 315 nm for 3, 7; 341 nm for 1, 2, 4, 5, 9, 10 and 370 nm for 6, 8, 11–13; PSS (*Z* → *E*): 370 nm for 3; 405 nm for 1, 4, 5, 7, 9, 10, 13 and 465 nm for 2, 6, 8, 11, 12).

a weak donor (2-naphthyl) differs from that of 7 which contains three relatively strong electron acceptor groups.

The X-ray structure of the *E*-isomer of benzoylpyridine hydrazone 7 (SI, Figures S105–S107 and Table S4) is consistent with findings from quantum-chemical calculations:³⁰ (a) the more stable rotamer of *E*-isomers exhibits the 180° rotation of the ketone pyridine ring compared to the *Z*-isomer; (b) the *E*-isomers are characterized by the approximately 60° mutual rotation of the aromatic rings on the ketone part of the molecule; with significant distortion of the ketone phenyl ring compared to the rest of the molecule (details in SI, section 2.4). Furthermore, we hypothesize that the close crystal packing due to intermolecular hydrogen bonds and slipped stack π – π interactions (SI, Figures S106–S107) is the driving force for rapid crystallization of the thermodynamically less

stable *E*-isomer from mother liquor containing both geometric isomers under ultrasound activation (see SI, the Synthesis section).

Photochemistry. The experimentally determined photoswitching parameters (Table 2) allow us to further investigate the structure–property trends of hydrazones 1–13. Interestingly, the hydrazine pyridyl ring not only improves the thermal stability but also increases the quantum yields (QYs) of both photochemical isomerizations (cf. hydrazones 1 and 7; SI, Figure S114). The observed moderate to good photoisomerization QYs depend on the solvent polarity, as discussed later. Hydrazone 7 exhibited 50 photochemical cycles with only a slight sign of photodegradation, or a competing photochemical reaction pathway (Figure 4; SI, Figure S115), thus demonstrating good photoswitching and high photosta-

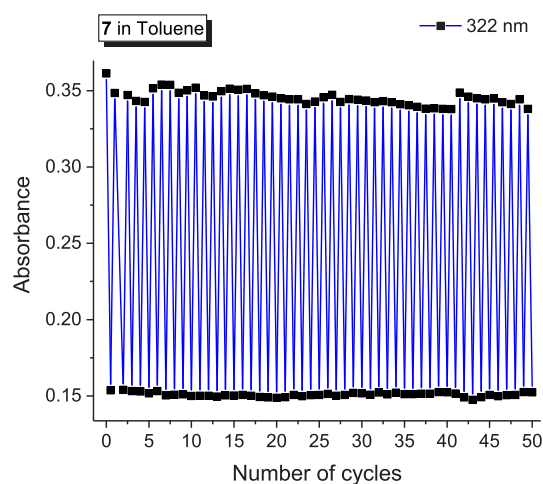


Figure 4. Photoswitching cycles of the 2-(*p*-nitrobenzoyl)pyridine hydrazone **7** in toluene during altered 315 and 405 nm LED irradiation to photostationary states (starting from pure *E*-isomer).

tionary state (PSS) photoconversion (>80%) in both polar and nonpolar solvents (Table 2; SI, Figures S122–S123). Analogous phenyl/2-pyridyl substitution in hydrazones **9/10** and **12/13** has also a positive albeit less pronounced effect on the *E*-to-*Z* photoisomerization QYs, while simultaneously lowering the *Z*-to-*E* photoisomerization QYs.

Our results show that increasing the EW character of the substituents on the hydrazone ring only leads to a slight increase in the efficiency of the *Z*-to-*E* photoisomerization (Table 2), whereas a steep increase of QYs can be observed in the case of the back *E*-to-*Z* photoisomerization (SI, Figure S114). One exception is the nitro hydrazone **6** with significantly lower efficiency of both *E*-to-*Z* and particularly

Z-to-*E* photoisomerizations (the nitro hydrazone **6** remains locked in the *Z* isomer structure). However, the incorporation of the nitro substituent to the chromophore structure often has a dramatic effect on the overall photophysics of a molecule, particularly due to the significant enhancement of the intersystem crossing rate.^{36,37} Moreover, in calculations, we also observed a low barrier (4 kcal/mol) for the excited-state intramolecular proton transfer, which may be another factor hindering the *Z*-to-*E* transformation of **6**. Substitution of the hydrazone phenyl ring with an 8-quinolinyl aromatic ring in hydrazone **8** leads to a reduction of its *Z*-to-*E* photoisomerization efficiency, in contrast to analogous ketoester hydrazones bearing a pyridyl ketone ring.¹⁷ Overall, the observed *E*-to-*Z* QYs are comparable to those of ketoester hydrazones^{17,18} and lower than those reported for pyridineacetyl hydrazones.²² Concerning the *Z*-to-*E* photoisomerization, our QYs are lower than those of the ketoester hydrazones possessing weaker intramolecular hydrogen bonding.¹⁸

Considering the absorption maxima λ_{\max} (Table 2), we observed that naphthoquinoline hydrazones **11–13** with enhanced π -conjugation showed the desired shift toward longer wavelengths while retaining a good isomer addressability. Moreover, these hydrazones exhibited higher *Z*-to-*E* photoisomerization QYs compared to parent pyridine hydrazone **1** and good to excellent PSS photoconversion. The bathochromic shift of the absorption maxima is particularly important for potential biological applications, and also laser/LED sources are more potent in the UVA/Vis region. Only recently, Aprahamian's group achieved a similar red shift of their core ketoester hydrazone structural motif by coplanarization of the ketone phenyl ring; however, the planarization in their isochromanone-like hydrazones resulted in the undesired reduction of thermal stability from hundreds

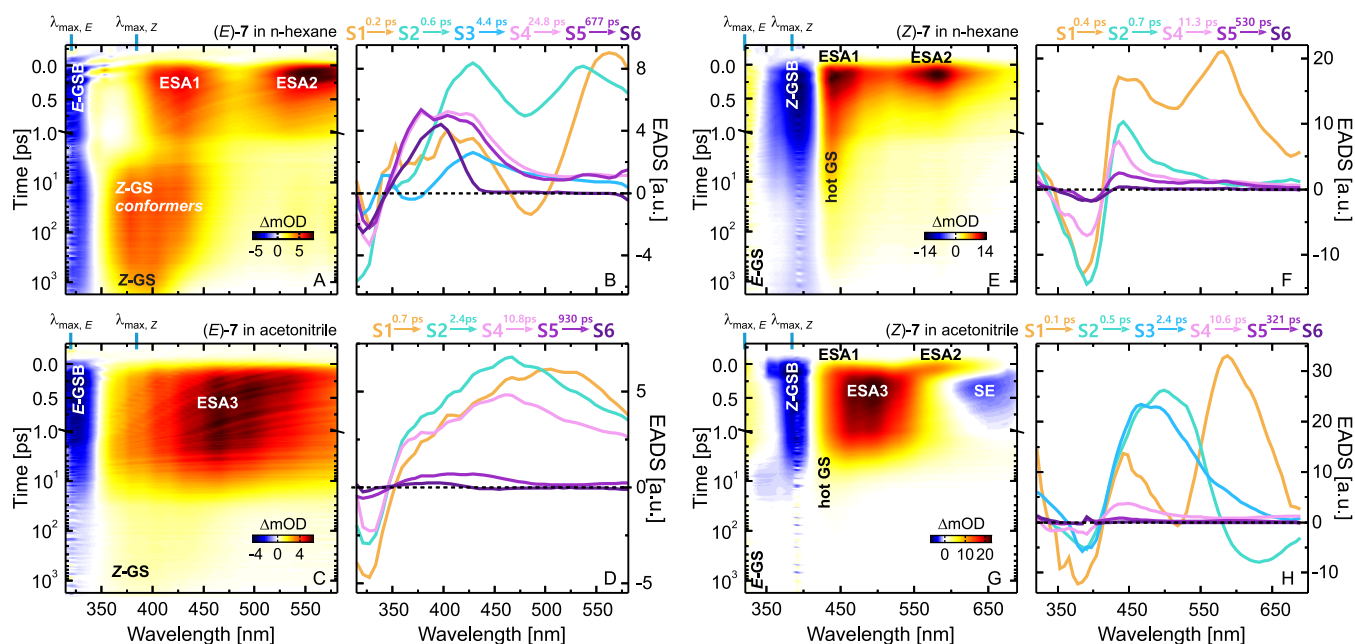


Figure 5. Transient absorption data and corresponding evolution-associated difference spectra (EADS) of the *E* (A–D)- and the *Z* (E–H)-isomers of hydrazone **7** measured in *n*-hexane (A, B, E, F) and acetonitrile (C, D, G, H) after $\pi\pi^*$ excitation (320 and 387 nm for *E* and *Z*, respectively). Negative absorption difference signals (light to dark blue) correspond to ground-state bleach (GSB) and stimulated emission (SE). Positive absorption difference signals (yellow through red to black) correspond to excited-state (ESA), hot ground-state (GS), and product absorption. For details on the pump–probe setup, see SI (section 3.5.1) and ref 38. For details on global target analysis, see the SI (section 3.5.2) and refs 39 and 40. See Figures S131–S134 for a comparison of the dynamics of **4** and **7**.

of years to days (~ 20 days).²¹ In our case, the thermal stability of naphthoylquinoline-based hydrazones ranges from 62 days (in a sterically hindered *E*-isomer of 1-naphthyl derivative **11**) to 6.5 years in the case of 2-naphthyl derivative **12** (Table 1). Particularly the 2-(naphthoyl)quinoline structural motif thus opens the way to the important subgroup of hydrazone photoswitches.

While a similar red shift can be observed for the nitro hydrazone **6**, the isomer addressability suffers significantly. Interestingly, the cyano derivatives **9** and **10** also feature a decrease in both the addressability and QYs compared to the parent hydrazones **1** and **7**.

To investigate the photochemistry of the presented 2-(*p*-nitrobenzoyl)pyridine hydrazones and explain the differences in the obtained quantum yields of both photochemical isomerizations, we combined ultrafast transient absorption spectroscopy and quantum-chemical calculations on the most promising hydrazone photoswitch **7**.

Ultrafast Photoconversion Dynamics. The kinetics of the ultrafast *E*-to-*Z* and *Z*-to-*E* photoisomerizations of **7** after excitation into the bright S_1 ($\pi\pi^*$) state are remarkably different in nonpolar (*n*-hexane) and polar (acetonitrile) solvents (Figure 5) despite the fact that the corresponding stationary absorption spectra are very similar (Figure S130). The detailed analysis of the transient absorption data is provided in the SI (section 3.5), while here we discuss our key findings.

In the case of *E*-to-*Z* photoisomerization of **7** in *n*-hexane, the transient absorption data below 1 ps is dominated by two ESA signatures (ESA1 and ESA2) belonging to the same initially excited S_1 state and the instantaneous ground state bleach (GSB) (Figure 5A). After ultrafast departure from the Franck–Condon (FC) region (200 fs), the S_1 state decays to the GS with a lifetime of about 600 fs (Figure 5B, EADS S1, S2, S3, see SI for a detailed discussion). The decay of the ES leads to the formation of a very broad GS absorption signature (350–475 nm) extending beyond the steady-state *Z*-isomer absorption band on both the lower and the higher energy side (Figure 5B, EADS S4). We assign this broad absorption to a population of metastable GS *Z* conformers such as L_1 and L_2 shown in Figure 2. The pool of *Z* conformers cools down with about 20 ps lifetime, as illustrated by the blue shift of the absorption (Figure 5B, EADS S4 \rightarrow S5), and finally relaxes with a lifetime of about 700 ps to the dominant most stable *Z* conformer (Figure 5B, EADS S5 \rightarrow S6). The strong nondecaying absorption difference signal composed of the *E*-isomer GSB and the *Z*-isomer absorption is in line with the high *E*-to-*Z* QY in *n*-hexane (16%; see Table S5).

The *E*-to-*Z* photoisomerization kinetics of **7** in acetonitrile (Figure 5C) clearly differs from that in *n*-hexane. We observe a single spectrally very broad ESA signature (labeled ESA3), which undergoes a blue shift on the sub-ps time scale (Figure 5D, EADS S1 \rightarrow S2). This is followed by a strongly distributed ES decay, as indicated by the relatively broad lifetime distribution centered at ~ 10 ps (Figure S132H) and the two similar EADS S1 and S2 (Figure 5D). The ES decay is accompanied by a strong recovery of the GSB signal (< 350 nm) and formation of a relatively weak, broad absorption band in the 350–475 nm range (Figure 5D, EADS S5). The broad absorption spectrum resembles the one observed in *n*-hexane, which we assigned to a pool of *Z* conformers (Figure S135). The decay of this pool to the thermodynamically stable *Z*-isomer occurs with a 900 ps lifetime in acetonitrile (Figure 5D,

EADS S5 \rightarrow S6). The significantly weaker *Z*-isomer product absorption in acetonitrile is in agreement with the reduced *E*-to-*Z* QY as compared to *n*-hexane (1.4%; see Table S5).

The transient absorption data from the *Z*-to-*E* photoisomerization in *n*-hexane bears some similarity to that of the *E*-to-*Z* direction. At early times (< 1 ps), we again observe two ESA signatures (ESA1 and ESA2) in addition to the GSB signal of the *Z*-isomer (385 nm). The ESA extends further to the higher energy spectral range and is clearly visible below 350 nm. Similar spectral signatures were observed in the ultrafast dynamics of ketoester hydrazones,⁴¹ albeit the ES decay kinetics in those compounds was significantly slower than what we observe here. The decay of the ES of (*Z*)-**7** occurs with a 400 fs lifetime (Figure 5F, EADS S1) and is associated with accumulation of hot GS signal (400–450 nm) and significant recovery of the GSB signal (350–450 nm). The cooling of the hot GS molecules continues on the ps time scale. Further, we detect additional GS dynamics (~ 500 ps, > 400 nm), which, based on our spectral analysis [see SI (section 3.5 and Figure S135)], we assign to the relaxation of a population of *Z*-isomer conformers (Figure 5F, EADS S5). At the end of our detection time scale, we observe the nondecaying GSB signal (< 400 nm) corroborating the high *Z*-to-*E* photoisomerization QY in *n*-hexane (9.4%; see Table S5).

In acetonitrile, the *Z*-to-*E* photoisomerization is markedly different (Figure 5G). After excitation, we observe the same ESA1 and ESA2 signatures as in *n*-hexane (~ 440 nm and ~ 580 nm). However, these ESAs are very short-lived and decay with a lifetime of about 100 fs (Figure 5H, EADS S1). Their decay is accompanied by similarly ultrafast rise of a strongly red-shifted stimulated emission (SE) signal (> 580 nm) and a new strong ESA signal (ESA3 at 500 nm) (Figure 5H, EADS S2). Concomitantly, the newly formed SE signal undergoes a very fast (500 fs) red shift (Figure 5H, EADS S2 \rightarrow S3), while the red edge of ESA3 undergoes a blue shift. The rise of a red-shifted emitting state for the *Z*-isomer in acetonitrile (as opposed to *n*-hexane) is also evident in the stationary fluorescence spectra (Figure S136). A comparison of EADS S1 for the experiments in *n*-hexane and acetonitrile (Figure 5F,H) reveals that in both solvents the initially excited S_1 ($\pi\pi^*$) states have a similar character. This is also supported by the relatively small difference in the stationary absorption spectra in the two solvents (Figure S130). However, the rise of a strongly red-shifted SE in acetonitrile is indicative of an ultrafast charge redistribution leading to the formation of an ES with charge-transfer (CT) character. The charge redistribution occurs simultaneously with the onset of the conformational changes that guide the molecule toward the conical intersection with the GS. The CT state in acetonitrile is further stabilized by solvent reorganization, which lowers the energy of the ES (SE red shift with 600 fs lifetime). Similar to the *E*-to-*Z* photoisomerization direction, the *Z*-isomer ES decay in acetonitrile is significantly slowed down as compared to *n*-hexane and occurs with a lifetime of ~ 2.5 ps (Figure 5H, EADS S3). Analogous to the experiments above, the ES decay is followed by cooling of the hot GS molecules (Figure 5H, EADS S4). The dynamics in acetonitrile ends with a nearly complete recovery of the GSB signal (at ~ 385 nm), which is in agreement with the strongly reduced *Z*-to-*E* QY in this solvent (2.2%; see Table S5).

Computational Insights into the Photochemistry. Focusing on low-lying excited states and comparing different levels

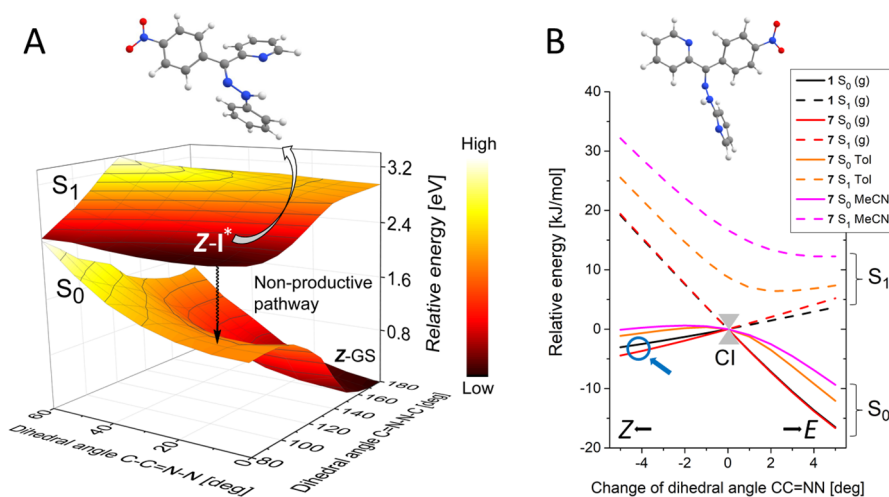


Figure 6. (A) Ground state and excited-state potential energy surfaces near the Z-isomer of the hydrazone **1**. Calculated as relaxed scan in the S_1 state at the ω B97XD/def2-SVPP level of theory in toluene. (B) Rigid scan of the potential energy surface in the vicinity of the MECI point. Calculated at the SF-TD-BHLYP/def2-SVPP level of theory.^{44,45}

of theory, an overall agreement between TD- ω B97X-D, wave function-based methods, and experiment was found, justifying the choice of the TD-DFT method for the analysis of ES potential energy surfaces far from the CI region. In particular, the theoretical $S_0 \rightarrow S_1$ excitation energy of the Z-isomer was consistently red-shifted with respect to that of the E-isomer, although both values tend to be blue-shifted compared to the experiment by about 0.5 and 0.1 eV, respectively (SI, Tables S6–S7). Importantly, the S_1 and S_2 ($n\pi^*$, dark) states in the Z-isomer were found to be more separated (~ 0.4 – 0.5 eV) compared to the E-isomer (~ 0.1 – 0.3 eV) (SI, Table S8 and Figure S137).

The photoisomerization in both directions proceeds via an excitation to the S_1 (bright, $\pi\pi^*$) state followed by a rotation around the N=C bond through a minimal energy conical intersection (MECI) point and further on the GS potential energy surface toward the product (see Video S3). In all benzoylpyridine hydrazones **1**–**10**, the E-to-Z photoisomerization is more efficient compared to the Z-to-E process. This can be rationalized in terms of different topologies of the S_1 potential energy surface of the E- and Z-isomers. While the E-to-Z isomerization via N=C rotation toward the MECI point is barrierless, for the Z-to-E isomerization, the relaxation via N=N rotation leads to a local minimum on the S_1 surface (metastable Z-I*) still being stabilized by a weak hydrogen bond (Figure 6A). In this geometry, the energy separation between S_1 and GS is less than 1.2 eV (~ 1000 nm), enabling the radiationless deactivation to the GS in the Z arrangement. This deactivation process constitutes a competitive non-productive pathway lowering the Z-to-E quantum yield. Recently, Wang et al.⁴² found the same torsional motion responsible for the nonemissive behavior of different Z-phenylhydrazone.

The observed differences in Z-to-E QYs between **1** and **7** can be mainly attributed to different hydrogen bond strengths in the ES. The hydrogen bond in (Z)-**7**-I* is longer (2.68 Å) and thus weaker, compared to the shorter contact (2.62 Å) found in (Z)-**1**-I*. In line with higher experimental QYs, the weaker (Z)-**7**-I* hydrogen bond presents a smaller barrier for Z-to-E photoisomerization.

The role of the intramolecular hydrogen bond was further examined by introducing quinoline in naphthoquinoline

hydrazones **11**–**13** (Scheme 2). The replacement of the ketone pyridyl with a less basic quinoline moiety was expected to facilitate the Z-to-E photoisomerization, and indeed, both the QYs and the PSS composition were improved (Table 2). However, it should be noted that the basicity of quinoline significantly increases upon the excitation, as was also previously shown experimentally,⁴³ and thus, the increase of QYs should not be simply attributed to the lower GS basicity of quinoline. In fact, unlike for pyridine acceptors, for (Z)-**13**, we theoretically observed spontaneous excited-state intramolecular proton transfer (ESIPT) from the NH group to the quinoline nitrogen. ESIPT leads to rehybridization of N–NH to N=N followed by a rotation around N=N and subsequent barrierless deactivation of the ES. By the involvement of the competitive nonradiative ESIPT pathway, the Z-to-E photoisomerization mechanism for naphthoquinoline hydrazones qualitatively differs from that for pyridyl-based derivatives.

Another aspect of the differences in the observed QYs is hidden in the topology around the MECI point (Figure 6B). Going from the excited-state E* through MECI, the transformation back to the E-isomer in the GS is favored by the slopes of the potential energy surface equally for both **1** and **7**. The potential energy slopes toward the Z-isomer, however, show that the E-to-Z isomerization should be more favorable for the photochrome **7** compared to **1** (Figure 6B, blue arrow). This is again consistent with the observed QYs (Table 2; SI, Figure S114). For the Z-to-E photoisomerization, the slopes of the potential energy surfaces are virtually identical for **1** and **7**, and as mentioned before, the QYs are predominantly influenced by the hydrogen bond strength in the metastable Z-I* ES intermediate.

In the ultrafast experiments, a broad strongly red-shifted SE signal was only observed for (Z)-**7** in acetonitrile (Figure 5). As a plausible SE source, we localized a very shallow minimum on the S_1 pathway between the FC region and Z-I*. The barrier protecting the minimum is less than 1 kcal/mol but has a clear physical explanation. The S_1 dipole moment in the FC geometry has a large value of 10.9 D and is further increased to 14.2 D in the minimum denoted as Z-SE. The subsequent disruption of the H-bond and distortion of the hydrazine part of the molecule is accompanied by a decrease of the dipole moment to 11.6 D in Z-I*. Whereas these changes do not

affect the formation of Z-I* in nonpolar solvents (toluene, *n*-hexane), they become important in polar acetonitrile, slowing down the relaxation of Z-FC to Z-I* and giving rise to the observed SE signal (Figure S138).

The involvement of the S_2 state in the *E*-to-*Z* isomerization cannot be fully excluded, in particular for **7**, in which the separation between S_1 and S_2 is less than 0.2 eV (SI, Table S7). In the trial ES molecular dynamics simulations, we observed the state switching between S_1 and S_2 . In addition, the MECI between S_1 and S_2 was located in the vicinity of the GS geometry. We calculated oscillator strengths between S_1 , S_2 , and the next 30 excited states. Although such a calculation has limitations, one clear result emerged: there were no transitions with significant oscillator strength between S_2 and the higher excited states. This means that, even if S_2 is involved in the photochemical transformations, it cannot be directly observed in the transient spectra (Figure 5). The modeled S_1 transient spectrum qualitatively follows the changes observed in the ultrafast experiments, e.g., the observed double-peak feature (SI, Figure S139) consistent with the ESA1/ESA2 signatures in Figure 5. The impact of the S_2 state population on QYs remains debatable, but given that (i) the separation of S_1 and S_2 increases with solvent polarity and a smaller QY was experimentally observed in MeCN compared to toluene, and (ii) the S_1 and S_2 separation in **1**, which has smaller QY, is larger than in **7**, the S_2 state could indeed act as a trap state affecting the photoisomerization QYs.

CONCLUSIONS

We designed and synthesized an extended series of substitutional derivatives of benzoylpyridine hydrazone photoswitches exhibiting extremely high thermal stability of the thermodynamically metastable isomer. The large variability of substituents enabled us to draw structure–property relationships for the kinetics of thermal back-isomerization as well as for the photoswitching parameters of this type of chromophores. Combining the quantum-chemical calculations and ultrafast transient absorption spectroscopy measurements, the photoswitching mechanism was elucidated, and the experimentally observed structure–property relationships were rationalized at the molecular level. The lead molecular skeleton based on the commercially available pyridyl hydrazine ring achieves an excellent thermal stability of 200 years and efficient photochemistry. Such a photoswitch may easily be anchored onto various surfaces or incorporated into biomolecules. The newly designed 2-(naphthoyl)quinoline analogs of 2-(benzoyl)pyridine hydrazones containing an extended π -conjugated moiety were shown to operate at the desired longer wavelengths, preserving the thermal stability of several years of the parent systems, which makes this family of photoswitches attractive for various applications including opto(bio)electronics and photopharmacology.

EXPERIMENTAL SECTION

General Methods. ^1H and ^{13}C NMR spectra were recorded at 600 or 300 MHz for ^1H nuclei and 151 or 75 MHz for ^{13}C nuclei. Chemical shifts are reported in δ units, parts per million (ppm); signals are referenced to TMS as an internal standard. Coupling constants (J) are given in hertz (Hz), and the multiplicity is abbreviated as s (singlet), d (doublet), dd (doublet of doublets), t (triplet), qd (quartet of doublets), and m (multiplet). Reactions were monitored by thin-layer chromatography (TLC) carried out on silica plates (Merck silica gel 60 F-254), visualized by irradiation with UV

light. Infrared spectra were recorded on a Nicolet 6700 FT-IR spectrometer (ATR technique). Commercially available reagents were used without further purification. The synthesis of starting materials was performed according to literature procedures or as specified below. HRMS spectra of compounds **2**, **4–6**, **8**, **10–13**, **15–17**, and **19–21** were measured on a Thermo Scientific Orbitrap Fusion Tribrid mass spectrometer (Thermo Fisher Scientific, Waltham, MA, USA) (orbital trap); equipped with a Dionex Ultimate 3000RS HPLC pump and Dionex Ultimate 3000RS autosampler. HRMS of compounds **3** and **9** was carried out on an Orbitrap Velos Pro Thermo Scientific, in instrument method FTMS (Fourier transformation) (orbital trap). Schemes of all prepared compounds, reaction schemes, full characterization of known compounds, and NMR spectra are shown in the Supporting Information.

Synthesis of Alcohols. (4-Nitrophenyl)(pyridin-2-yl)methanol (**14**), 4-(hydroxy(pyridin-2-yl)methyl)benzotrile (**15**), naphthalen-1-yl(quinolin-2-yl)methanol (**16**), and naphthalen-2-yl(quinolin-2-yl)methanol (**17**) were synthesized according to the previously published method described in ref 29. A detailed description is shown in the Supporting Information.

Synthesis of Ketones. (4-Nitrophenyl)(pyridin-2-yl)methanone (**18**), 4-picolinoylbenzotrile (**19**), naphthalen-1-yl(quinolin-2-yl)methanone (**20**), and naphthalen-2-yl(quinolin-2-yl)methanone (**21**) were synthesized according to the previously published method described in ref 29. A detailed description is shown in the Supporting Information.

Synthesis of Hydrazones. General Approach. Hydrazine (0.81 mmol) was added to a stirred solution of ketone (0.81 mmol) and AcOH (0.2 mL) in EtOH (8 mL) in one portion. The reaction mixture was refluxed 5–18 h (depends on reactivity of ketone). The reaction progress was monitored by TLC. After a specified time, the reaction mixture was cooled to room temperature. Precipitate crystals of hydrazones **1**, **3**, **4**, **6**, **7**, **8**, **9**, and **10** (excluding hydrazones **11**, **12**, **13**, and **14**, which do not precipitate from the reaction mixture) were filtered off from the reaction mixture. The filtrate (reaction mixture) was then concentrated under reduced pressure and dissolved in CHCl_3 (25 mL). This organic phase was washed by distilled water (2 \times 10 mL), and the organic layer was dried over anhydrous Na_2SO_4 . Then the solvent was removed by distillation under reduced pressure, and the crude reaction mixture was analyzed by TLC. If TLC analysis showed marks for products, the concentrated organic phase was purified by flash chromatography (for chromatography conditions, see the characterization of hydrazones below).

General Method for the Synthesis of Hydrazones 2 and 5. Na_2CO_3 (0.81 mmol) was added to a stirred solution of hydrazine hydrochloride (0.81 mmol) in EtOH (8 mL), and the mixture was stirred for 5 min. After that, ketone (0.81 mmol) and AcOH (0.2 mL) were added, and the reaction mixture was refluxed 18 h (depends on the reactivity of the ketone). The reaction mixture was next concentrated by distillation under reduced pressure and dissolved in CHCl_3 (30 mL). The organic phase was washed by distilled water (2 \times 15 mL), and the organic layer was dried over anhydrous Na_2SO_4 . Then the solvent was removed by distillation under reduced pressure, and the crude reaction mixture was purified by flash chromatography (for chromatography conditions, see the characterization of hydrazones below).

Alternative Synthetic Procedure of (E)-Isomers for Hydrazones 1 and 7. Phenylhydrazine (0.1 mL) was added in one portion to a solution of ketone (0.81 mmol) and AcOH (0.5 mL) in EtOH in an active ultrasonic bath (25 W; 50 Hz) at room temperature. The reaction mixture was then exposed to ultrasound waves for 20 min. The temperature of the bath was maintained not to exceed 25 $^\circ\text{C}$. Sonification at room temperature thus leads to the precipitation of the thermodynamically less stable *E*-isomer for hydrazone **1**. The precipitate was then filtered and washed with cold EtOH. Hydrazone **7** did not precipitate during the action of ultrasound waves, so the crude reaction mixture was allowed to stand at room temperature for 3 h; precipitated crystals were filtered ((*E*)-**7**, 38% yield).

(*E*)-2-((4-Nitrophenyl)(2-phenylhydrazone)methyl)pyridine (**1**).²⁹
(*Z*)-2-((4-Nitrophenyl)(2-phenylhydrazone)methyl)pyridine (**1**): iso-

lated by gradient flash chromatography on silica (SiO₂, hexanes/EtOAc (2:1) to pure EtOAc), (Z)-1; red solid; mp = 150–152 °C; ¹H NMR (600 MHz, DMSO-*d*₆) δ 11.89 (s, 1H), 8.87 (ddd, *J* = 5.1 Hz, 1.7 Hz, 0.9 Hz, 1H), 8.25 (d, *J* = 8.8 Hz, 2H), 8.01 (ddd, *J* = 7.8 Hz, 7.8 Hz, 1.4 Hz, 1H), 7.76 (d, *J* = 8.8 Hz, 2H), 7.56 (ddd, *J* = 7.6 Hz, 4.9 Hz, 1.0 Hz, 1H), 7.46 (d, *J* = 7.9 Hz, 1H), 7.36–7.24 (m, 1H), 6.89 (ddd, *J* = 6.4 Hz, 6.4 Hz, 1.9 Hz, 1H) ppm; ¹³C{H} NMR (151 MHz, DMSO-*d*₆) δ 152.0, 149.9, 146.7, 145.4, 141.0, 138.3, 137.2, 129.6, 128.5, 124.3, 124.1, 121.3, 120.2, 114.0 ppm; IR $\tilde{\nu}_{\max}$ 3100 (w, N—H), 3024 (w, C—H), 2820 (w, C—H), 1586 (m, C=N), 1564 (m, C=C), 1506 (s, C=C) 1336 (s, C=C), 1240 (m, C—N), 1147 (s), 1107 (m), 855 (s, C—H), 713 (s, C—H) cm⁻¹.

(E)-2-((2-(4-Methoxyphenyl)hydrazineylidene)(4-nitrophenyl)methyl)pyridine (2): isolated by filtration from the reaction mixture; overall yield = 149 mg (43%); orange solid; (E)-2 mp = 171–173 °C; ¹H NMR (600 MHz, CDCl₃) δ 8.43 (d, *J* = 8.7 Hz, 2H), 8.44–8.42 (m, 1H), 8.22 (ddd, *J* = 8.1 Hz, 1.1 Hz, 1.1 Hz, 1H), 7.73 (ddd, *J* = 8.1 Hz, 8.0 Hz, 1.1 Hz, 1H), 7.59 (d, *J* = 8.7 Hz, 2H), 7.55 (bs, 1H), 7.16 (ddd, *J* = 8.1 Hz, 7.5 Hz, 1.1 Hz, 0H), 7.07 (d, *J* = 8.9 Hz, 2H), 6.87 (d, *J* = 8.9 Hz, 2H), 3.79 (s, 3H) ppm; ¹³C{H} NMR (151 MHz, CDCl₃) δ 153.1, 151.8, 146.2, 145.3, 136.6, 134.8, 133.7, 128.2, 122.3, 122.2, 119.9, 117.7, 112.0, 111.8, 53.1 ppm; IR $\tilde{\nu}_{\max}$ 2959 (w, N—H), 2903 (w, C—H), 1590 (w, C—H), 1556 (m, C=N), 1508 (s), 1465 (s, C=C) 1426 (s, C=C), 1224 (m, C—N), 1030 (s), 997 (m), 831 (s, C—H), 782 (s, C—H), 703 (m) cm⁻¹; HRMS (ESI) *m/z* calcd for C₁₉H₁₆N₄O₃⁺ ([M + H]⁺) found 349.1294, calcd C₁₉H₁₆N₄O₃⁺ ([M + H]⁺) 349.1295. Elemental analysis calcd for C₁₇H₁₃N₃O₂: C, 74.43; H, 5.14; N, 20.42%. Found: C, 74.52; H, 5.29; N, 20.33%.

(Z)-2-((4-Nitrophenyl)-(2-(perfluorophenyl)hydrazineylidene)methyl)pyridine (3): isolated by filtration; overall yield = 200 mg (61%); yellow solid (Z)-3 mp = 200–202 °C; ¹H NMR (600 MHz, DMSO-*d*₆) δ 13.03 (bs, 1H); 8.85 (ddd, *J* = 4.9 Hz, 1.7 Hz, 0.8 Hz, 1H); 8.28 (d, *J* = 8.9 Hz, 2H); 8.03 (ddd, *J* = 7.9 Hz, 7.84 Hz, 1.8 Hz, 1H); 7.75 (d, *J* = 8.9 Hz, 2H); 7.59 (ddd, *J* = 7.6 Hz, 4.9 Hz, 1.0 Hz, 1H); 7.42 (d, *J* = 8.0 Hz, 1H) ppm; ¹H NMR (600 MHz, CDCl₃) δ 13.55 (s, 1H), 8.80 (d, *J* = 4.6 Hz, 1H), 8.27 (d, *J* = 8.8 Hz, 2H), 7.85 (ddd, *J* = 7.9 Hz, 7.8 Hz, 1.6 Hz, 1H), 7.77 (d, *J* = 8.8 Hz, 2H), 7.42 (dd, *J* = 7.2 Hz, 5.2 Hz, 1H), 7.36 (d, *J* = 8.1 Hz, 1H) ppm; ¹³C{H} NMR (151 MHz, CDCl₃) δ 152.2, 148.0, 147.5, 144.4, 139.6, 138.3 (ddd, *J* = 248 Hz, 14.1, 3.7 Hz), 137.4, 135.7 (ddd, *J* = 248, 14, 3.7 Hz), 129.4, 124.7, 123.9, 123.7, 120.4 (dd, *J* = 9.4, 2.9, 1.7), ppm; ¹⁹F NMR (564 MHz, CDCl₃) δ -156.42 (dddd, *J* = 20.7 Hz, 4.2 Hz, 4.2 Hz, 2.3 Hz, 2F), -163.41 (ddd, *J* = 21.2 Hz, 21.2 Hz, 5 Hz, 2F) -166.72 (dddd, *J* = 21.84 Hz, 21.84 Hz, 4.18 Hz, 4.18 Hz, 1F) ppm; IR $\tilde{\nu}_{\max}$ 1739 (w), 1574 (w), 1508 (m), 1342 (m), 1216 (m), 1138 (m), 974 (s), 861 (s), 796 (s), 697 (s), 566 (m) cm⁻¹; HRMS (ESI) *m/z* for C₁₈H₉F₃N₄O₂⁺ ([M + H]⁺) found 409.0717, calcd C₁₈H₉F₃N₄O₂⁺ ([M + H]⁺) 409.0718.

(E)-2-((4-Nitrophenyl)-(2-(4-(trifluoromethyl)phenyl)hydrazineylidene)methyl)pyridine (4): isolated by gradient flash chromatography on silica (SiO₂, hexanes/EtOAc (2:1) to pure EtOAc); overall yield = 110 mg (35%); 50 mg of orange solid; (E)-4 mp = 166–169 °C; ¹H NMR (600 MHz, CDCl₃) δ 8.47–8.44 (m, 3H); 8.24 (ddd, *J* = 8.1 Hz, 1.1 Hz, 1.1 Hz, 2H); 7.82 (ddd, *J* = 7.92 Hz, 7.91 Hz, 1.7 Hz, 1H); 7.74 (bs, 1H); 7.23 (ddd, *J* = 7.4 Hz, 4.9 Hz, 1.2 Hz, 2H); 7.18 (d, *J* = 8.5 Hz, 1H); 7.39 (ddd, *J* = 7.6 Hz, 4.9 Hz, 1.1 Hz, 1H); 7.35 (ddd, *J* = 8.12 Hz, 1.02 Hz, 1.02 Hz, 1H), 7.31 (d, *J* = 8.5 Hz, 1H) ppm; ¹³C{H} NMR (151 MHz, DMSO-*d*₆) δ 155.9, 148.9, 148.4, 147.9, 148.1, 143.6, 140.7, 137.1, 126.7 (q, *J* = 3.9 Hz), 124.7, 124.3, 123.4, 120.6, 120.4 (q, *J* = 31.7 Hz), 113.7 ppm; IR $\tilde{\nu}_{\max}$ 3309 (w, N—H), 2955 (w, C—H), 2920 (w, C—H), 1613 (m, C=N), 1597 (m, C=C), 1512 (m, C=C) 1317 (s, C=C), 1257 (s), 1099 (s), 1061 (s), 835 (s), 780 (s), 701 (s) cm⁻¹; HRMS (ESI) *m/z* for C₁₉H₁₃F₃N₄O₂⁺ ([M + H]⁺) found 387.1063, calcd C₁₉H₁₃F₃N₄O₂⁺ ([M + H]⁺) 387.1063. ¹H NMR (600 MHz, DMSO-*d*₆) mixture of isomers Z/E (2:1) δ 11.85 (s, 1H), 9.80 (s, 0.5H), 8.86 (d, *J* = 4.3 Hz, 1H), 8.36 (d, *J* = 8.3 Hz, 1.5H), 8.24 (d, *J* = 8.7 Hz, 2H), 8.22 (d, *J* = 8.1 Hz, 0.5H), 8.01 (ddd, *J* = 7.8, 7.8 Hz, 1.8 Hz, 1H), 7.86 (ddd, *J* = 7.9, 7.9 Hz, 1.7 Hz, 0.5H), 7.75 (d, *J* = 8.6

H_z, 2H), 7.65–7.53 (m, 5H), 7.47–7.42 (m, 4H), 7.30 (dd, *J* = 7.4 Hz, 4.9 Hz, 0.5H) ppm.

(Z)-2-((4-Nitrophenyl)-(2-(4-(trifluoromethyl)phenyl)hydrazineylidene)methyl)pyridine (4): isolated by gradient flash chromatography on silica (SiO₂, hexanes:EtOAc (2:1) to pure EtOAc); overall yield = 110 mg (35%); orange solid; 60 mg of (Z)-4 mp = 140–142 °C; ¹H NMR (600 MHz, CDCl₃) δ 13.58 (bs, 1H); 8.82 (ddd, *J* = 5.0 Hz, 1.8 Hz, 0.9 Hz, 1H); 8.29 (d, *J* = 8.8 Hz, 2H); 7.82 (ddd, *J* = 7.98 Hz, 7.89 Hz, 1.8 Hz, 1H); 7.79 (d, *J* = 8.8 Hz, 2H); 7.55 (d, *J* = 8.5 Hz, 1H); 7.39 (ddd, *J* = 7.6 Hz, 4.9 Hz, 1.1 Hz, 1H); 7.35 (ddd, *J* = 8.12 Hz, 1.02 Hz, 1.02 Hz, 1H), 7.31 (d, *J* = 8.5 Hz, 1H) ppm; ¹³C{H} NMR (151 MHz, DMSO-*d*₆) δ 151.8, 150.2, 147.9, 147.1, 144.8, 143.7, 140.0, 138.4, 131.7, 128.7, 126.9 (q, *J* = 3.9 Hz), 125.5, 124.2, 120.9 (q, *J* = 31.7 Hz) 113.9 ppm; IR $\tilde{\nu}_{\max}$ 2917 (w, N—H), 2635 (w, C—H), 1613 (m, C=N), 1528 (m), 1503 (s), 1314 (s), 1101 (s), 1060 (s), 832 (s), 793 (s), 614 (s) cm⁻¹; HRMS (ESI) *m/z* for C₁₉H₁₃F₃N₄O₂⁺ ([M + H]⁺) found 387.1063, calcd C₁₉H₁₃F₃N₄O₂⁺ ([M + H]⁺) 387.1063.

(E)-4-2-((4-Nitrophenyl)(pyridin-2-yl)methylene)hydrazineylidenebenzotrile (5): isolated by flash chromatography on silica (SiO₂, hexanes/EtOAc (2:1)); overall yield = 150 mg (54%); pale yellow solid; (E)-5 mp = 239–241 °C; ¹H NMR (300 MHz, DMSO-*d*₆) δ 9.94 (s, 1H), 8.44–8.34 (m, 3H), 8.25 (d, *J* = 8.1 Hz, 1H), 7.89 (ddd, *J* = 8.0 Hz, 7.9 Hz, 1.6 Hz, 1H), 7.67 (d, *J* = 5.3 Hz, 2H), 7.64 (d, *J* = 5.3 Hz, 2H), 7.42 (d, *J* = 8.8 Hz, 2H), 7.33 (ddd, *J* = 7.5 Hz, 4.8 Hz, 1.1 Hz, 1H) ppm; ¹H NMR (600 MHz, CDCl₃) δ 8.46 (d, *J* = 8.6 Hz, 2H), 8.23 (d, *J* = 8.1 Hz, 1H), 7.86–7.74 (m, 2H), 7.58 (d, *J* = 8.6 Hz, 1H), 7.56 (d, *J* = 8.7 Hz, 1H), 7.25–7.23 (m, 1H), 7.16 (d, *J* = 8.7 Hz, 1H) ppm; ¹³C{H} NMR (151 MHz, CDCl₃) δ 153.8, 148.0, 147.4, 145.7, 143.9, 137.2, 135.4, 132.8, 129.5, 123.7, 122.3, 119.7, 118.5, 112.5, 102.7 ppm; IR $\tilde{\nu}_{\max}$ 3080 (w, N—H), 2213 (m, C≡N), 1569 (m, C=N), 1508 (s), 1349 (s), 1243 (m), 1132 (s) 1104 (s), 857 (s), 792 (s), 542 (s) cm⁻¹; HRMS (ESI) *m/z* for C₁₉H₁₃N₅O₂⁺ ([M + H]⁺) found 344.1141, calcd C₁₉H₁₃N₅O₂⁺ ([M + H]⁺) 344.1142.

2-((4-Nitrophenyl)-(2-phenylhydrazono)methyl)pyridine (6): isolated by filtration of precipitated crystals from the reaction mixture; overall yield = 60%, mixture of isomers ¹H NMR, mixture of isomers ([E/Z]/[3:1] ratio) (600 MHz, DMSO-*d*₆) δ 11.98 (s, 1H, Z-isomer), 10.18 (s, 1H, E-isomer), 8.87 (ddd, *J* = 4.9 Hz, 1.8 Hz, 1 Hz, 1H, Z-isomer), 8.40–8.36 (m, 3H for E-isomer), 8.25–8.24 (m, 2H, Z-isomer, overlap with 8.25 signal), 8.25 (d, *J* = 7.6 Hz, 1H, E-isomer), 8.18–8.12 (m, 2H, Z-isomer); 8.14 (d, *J* = 9.2 Hz, 2H, E-isomer), 8.03 (ddd, *J* = 7.81 Hz, 7.77 Hz, 1.8 Hz, 1H, Z-isomer), 7.89 (ddd, *J* = 9.4 Hz, 7.9 Hz, 1.7 Hz, 1H, E-isomer); 7.76 (d, *J* = 8.9 Hz, 2H, Z-isomer), 7.64 (d, *J* = 8.7 Hz, 2H, E-isomer), 7.62–7.58 (m, 1H, Z-isomer), 7.50–7.42 (m, 2H for E-isomer, 3H for Z-isomer), 8.34 (ddd, *J* = 7.5, 4.9, 1.2 Hz, 1H, E-isomer) ppm; ¹³C{H} NMR (151 MHz, DMSO-*d*₆) δ 155.5, 151.5, 150.9, 150.4, 149.0, 148.2, 147.4, 146.2, 144.3, 142.5, 140.4, 140.3, 140.1, 138.5, 137.2, 131.7, 128.9, 126.2, 126.1, 125.7, 125.0, 124.3, 124.2, 123.8, 121.0, 113.6, 113.4 ppm.

(E)-2-((4-Nitrophenyl)-(2-(4-nitrophenyl)hydrazineylidene)methyl)pyridine (6): isolated by flash chromatography on silica (eluent = hexanes/EtOAc (3:1)), (E)-6; pale yellow solid; mp = 243–245 °C; ¹H NMR (600 MHz, DMSO-*d*₆) δ 10.19 (s, 1H), 8.50–8.33 (m, 3H), 8.28 (ddd, *J* = 8.1 Hz, 1.0 Hz, 1.0 Hz, 1H), 8.16 (d, *J* = 9.2 Hz, 2H), 7.91 (ddd, *J* = 8.1 Hz, 7.5 Hz, 1.9 Hz, 1H), 7.67 (d, *J* = 8.7 Hz, 2H), 7.46 (d, *J* = 9.2 Hz, 2H), 7.36 (ddd, *J* = 7.5 Hz, 4.7 Hz, 1.0 Hz, 1H) ppm; ¹³C{H} NMR (151 MHz, DMSO-*d*₆) δ 155.6, 150.9, 149.1, 148.2, 146.2, 140.3, 140.1, 137.2, 131.7, 126.2, 124.3, 123.9, 121.0, 113.5 ppm; IR $\tilde{\nu}_{\max}$ 2920 (w, N—H), 2851 (w), 1735 (w, N=C), 1591 (m), 1560 (m) 1257 (s, C=C), 1089 (s), 1013 (s), 789 (s), 748 (m), 695 (m), 490 (m) cm⁻¹; HRMS (ESI) *m/z* for C₁₈H₁₃N₅O₄⁺ ([M + H]⁺) found 364.1039, calcd C₁₈H₁₃N₅O₄⁺ ([M + H]⁺) 364.1040.

(E)-2-((4-Nitrophenyl)-(2-(pyridin-2-yl)hydrazineylidene)methyl)pyridine (7): isolated by filtration of reaction mixture (ultrasound condition); overall yield = 100 mg (38%); pale yellow solid (E)-7 mp = 199–203 °C; ¹H NMR (600 MHz, DMSO-*d*₆) δ 9.47 (s, 1H), 8.39

(ddd, $J = 4.8$ Hz, 1.8 Hz, 0.9 Hz, 1H), 8.35 (d, $J = 8.8$ Hz, 2H), 8.24 (d, $J = 8.2$ Hz, 1H), 8.10 (ddd, $J = 4.9$ Hz, 1.8 Hz, 0.8 Hz, 1H), 8.87 (ddd, $J = 8.0$ Hz, 7.5 Hz, 1.8 Hz, 1H), 7.72 (ddd, $J = 8.2$ Hz, 7.3 Hz, 1.9 Hz, 1H), 7.62 (d, $J = 8.8$ Hz, 2H), 7.47 (d, $J = 8.2$ Hz, 1H), 7.31 (ddd, $J = 7.4$ Hz, 4.8 Hz, 1.1 Hz, 1H), 6.86 (ddd, $J = 7.2$ Hz, 4.9 Hz, 1.0 Hz, 1H) ppm; $^{13}\text{C}\{\text{H}\}$ NMR (151 MHz, DMSO- d_6) δ 156.8, 155.8, 148.9, 148.1, 148.1, 143.9, 140.3, 138.7, 137.1, 131.5, 124.4, 123.5, 120.6, 117.0, 107.9 ppm; IR $\tilde{\nu}_{\text{max}}$ 2999 (w, N—H), 2930 (w, C—H), 2088 (w, C—H), 1594 (m, C=N), 1566 (s, C=C), 1508 (s, C=C) 1421 (s, C=C), 1295 (m, C—N), 1128 (s), 1084 (m), 847 (m, C—H), 771 (s, C—H), 704 (s), 679 (s) cm^{-1} . Elemental analysis calcd for $\text{C}_{17}\text{H}_{13}\text{N}_3\text{O}_2$: C, 74.43; H, 5.14; N, 20.42%. Found: C, 74.48; H, 5.18; N, 20.32%.

(Z)-2-((4-Nitrophenyl)(2-(pyridin-2-yl)hydrazineylidene)methyl)pyridine (7): isolated by flash chromatography on silica (eluent: EtOAc); overall yield = 178 mg (66%); orange solid, (Z)-7 mp 133–136 °C; ^1H NMR (600 MHz, DMSO- d_6) δ 12.86 (bs, 1H), 8.91 (ddd, $J = 4.9$ Hz, 1.8 Hz, 0.8 Hz, 1H), 8.29 (d, $J = 8.7$ Hz, 2H), 8.20 (ddd, $J = 4.9$ Hz, 1.8 Hz, 0.8 Hz, 1H), 8.02 (ddd, $J = 7.9$ Hz, 7.8 Hz, 1.8 Hz, 1H), 7.86 (d, $J = 8.7$ Hz, 2H), 7.76 (ddd, $J = 8.8$ Hz, 7.3 Hz, 1.8 Hz, 1H), 7.59 (ddd, $J = 7.5$ Hz, 4.9 Hz, 0.8 Hz, 1H), 7.47–7.41 (m, 2H); 6.94 (ddd, $J = 7.4$ Hz, 4.9 Hz, 0.9 Hz, 1H) ppm; $^{13}\text{C}\{\text{H}\}$ NMR (151 MHz, DMSO- d_6) δ 156.5, 151.9, 149.3, 148.4, 147.3, 145.0, 138.9, 138.5, 138.4, 129.7, 125.5, 124.7, 124.1, 117.5, 107.5 ppm; IR $\tilde{\nu}_{\text{max}}$ 2922 (w, N—H), 2294 (w), 1591 (w), 1566 (m), 1506 (s), 1486 (s), 1422 (s), 1298 (s), 1086 (s), 1 (m), 847 (s, C—H), 733 (s, C—H), 577 (s) cm^{-1} . Elemental analysis calcd for $\text{C}_{17}\text{H}_{13}\text{N}_5\text{O}_2$: C, 74.43; H, 5.14; N, 20.42%. Found: C, 74.52; H, 5.29; N, 20.33%.

(E)-8-2-((4-Nitrophenyl)(pyridin-2-yl)methylene)hydrazineylidenequinoline (8): isolated by filtration; overall yield = 180 mg (50%); yellow solid; (E)-8 mp = 178–181 °C; ^1H NMR (300 MHz, DMSO- d_6) δ 9.73 (bs, 1H); 8.62 (dd, $J = 4.1$ Hz, 1.3 Hz, 1H); 8.47 (d, $J = 8.6$ Hz, 2H); 8.42 (ddd, $J = 5.2$ Hz, 1.3 Hz, 0.5 Hz, 1H); 8.36 (d, $J = 8.2$ Hz, 1H); 8.31 (dd, $J = 8.4$ Hz, 1.7 Hz, 1H); 7.91 (ddd, $J = 7.67$ Hz, 7.53 Hz, 1.82 Hz, 1H); 7.85–7.77 (m, 1H), 7.78 (d, $J = 8.6$ Hz, 2H); 7.59 (dd, $J = 7.9$ Hz, 7.9 Hz, 1H), 7.50 (dd, $J = 8.4$ Hz, 4.2 Hz, 1H); 7.44 (d, $J = 8.0$ Hz, 1H); 7.34 (ddd, $J = 7.3$ Hz, 4.5 Hz, 0.9 Hz, 1H) ppm; $^{13}\text{C}\{\text{H}\}$ NMR (151 MHz, DMSO- d_6) δ 155.6, 149.0, 148.9, 148.2, 144.4, 139.8, 139.0, 137.2, 136.7, 136.4, 131.5, 128.5, 128.0, 124.8, 123.5, 122.6, 120.7, 118.9, 109.0 ppm; IR $\tilde{\nu}_{\text{max}}$ 3100 (w, N—H), 1739 (w, C—H), 1577 (w, C=C), 1557 (m, C=N), 1517 (s, C=C), 1428 (s, C=C) 1316 (s, C=C), 1204 (m, C—N), 1134 (m), 1107 (m), 994 (m, C—H), 858 (m), 757 (s, C—H), 792 (m), 702 (m) cm^{-1} ; HRMS (ESI) m/z for $\text{C}_{21}\text{H}_{15}\text{N}_5\text{O}_2^+$ ($[\text{M} + \text{H}]^+$) found 370.1297, calcd $\text{C}_{21}\text{H}_{15}\text{N}_5\text{O}_2^+$ ($[\text{M} + \text{H}]^+$) 370.1299.

(E)-4-((2-Phenylhydrazineylidene)(pyridin-2-yl)methyl)benzonitrile (9): isolated by filtration from reaction mixture; overall yield = 76%; yellow solid (E)-9 mp = 180–183 °C; ^1H NMR (600 MHz, CDCl_3) δ 8.37 (d, $J = 4.9$ Hz, 1H), 8.16 (d, $J = 8.1$ Hz, 1H), 7.81 (d, $J = 8.2$ Hz, 1H), 7.67 (ddd, $J = 8.0$ Hz, 8.0 Hz, 1.7 Hz, 1H), 7.56 (s, 1H), 7.45 (d, $J = 8.2$ Hz, 1H), 7.22 (dd, $J = 7.9$ Hz, 7.9 Hz, 2H), 7.11 (dd, 7.5 Hz, 4.9 Hz), 7.05 (d, $J = 7.9$ Hz, 2H), 6.86 (dd, $J = 7.3$ Hz, 7.3, 1H) ppm; $^{13}\text{C}\{\text{H}\}$ NMR (151 MHz, CDCl_3) δ 155.7, 148.7, 143.7, 141.8, 137.0, 136.2, 133.1, 130.4, 129.4, 122.5, 121.3, 120.4, 118.4, 113.3, 113.1 ppm; IR $\tilde{\nu}_{\text{max}}$ 3053 (w), 2226 (w), 1599 (m), 1561 (m), 1428 (s) 1241 (s), 1129 (m), 996 (m), 898 (m), 761 (s) cm^{-1} ; HRMS (ESI) m/z for $\text{C}_{19}\text{H}_{14}\text{N}_4^+$ ($[\text{M} + \text{H}]^+$) found 299.1291, calcd $\text{C}_{19}\text{H}_{14}\text{N}_4^+$ ($[\text{M} + \text{H}]^+$) 299.1291.

(Z)-4-((2-Phenylhydrazineylidene)(pyridin-2-yl)methyl)benzonitrile (9): isolated by flash chromatography on silica (SiO_2 , eluent: CH_2Cl_2); overall yield = 76%; orange solid, (Z)-9 mp = 110–112 °C; ^1H NMR (600 MHz, CDCl_3) δ 13.19 (s, 1H), 8.71 (d, $J = 4.5$ Hz, 1H), 7.71 (ddd, $J = 7.8$ Hz, 7.8 Hz, 1.6 Hz), 7.66 (d, $J = 8.2$ Hz, 2H), 7.62 (d, $J = 8.2$ Hz, 2H), 7.30–7.21 (m, 4H), 7.19–7.18 (m, 2H), 6.87 (dd, $J = 7.1$ Hz, 7.1 Hz, 1H) ppm; $^{13}\text{C}\{\text{H}\}$ NMR (151 MHz, CDCl_3) δ 152.9, 148.0, 144.1, 143.8, 137.0, 135.0, 132.1, 129.3, 129.2, 124.3, 122.8, 121.3, 119.1, 113.7, 110.8 ppm; IR $\tilde{\nu}_{\text{max}}$ 3000 (w), 2222 (w), 1597 (m), 1521 (m), 11497 (m), 1238 (m), 1134 (s), 852 (m), 791 (m), 753 (m) cm^{-1} ; HRMS (ESI) m/z for $\text{C}_{19}\text{H}_{14}\text{N}_4^+$ ($[\text{M} + \text{H}]^+$) found 299.1291, calcd $\text{C}_{19}\text{H}_{14}\text{N}_4^+$ ($[\text{M} + \text{H}]^+$) 299.1291.

(E)-4-(Pyridin-2-yl(2-(pyridin-2-yl)hydrazineylidene)methyl)benzonitrile (10): isolated by filtration from reaction mixture; overall yield = 71%; colorless solid; (E)-10 mp = 200–203 °C; ^1H NMR (600 MHz, CDCl_3) δ 8.40 (ddd, $J = 4.9$ Hz, 1.8 Hz, 0.9 Hz, 1H), 8.13 (d, $J = 8.1$ Hz, 2H), 8.04 (ddd, $J = 5.7$ Hz, 1.7 Hz, 0.8 Hz, 1H), 7.69 (ddd, $J = 8.1$ Hz, 7.5 Hz, 1.8 Hz, 1H), 7.63–7.58 (m, 1H), 7.44 (d, $J = 8.2$ Hz, 3H), 7.17–7.12 (m, 1H), 6.78 (ddd, $J = 7.2$ Hz, 4.9 Hz, 1.0 Hz, 1H) ppm; $^{13}\text{C}\{\text{H}\}$ NMR (151 MHz, CDCl_3) δ 155.8, 155.3, 147.8, 143.8, 138.3, 136.8, 136.3, 133.2, 133.3, 123.0, 120.6, 118.3, 117.0, 113.3, 107.7 ppm; IR $\tilde{\nu}_{\text{max}}$ 3158 (w), 2228 (w), 1595 (m), 1561 (m), 1502 (m) 1422 (s), 1295 (s), 1130 (s), 988 (s), 843 (s), 769 (s), 516 (m); HRMS (ESI) m/z for $\text{C}_{18}\text{H}_{13}\text{N}_5^+$ ($[\text{M} + \text{H}]^+$) found 300.1244, calcd $\text{C}_{18}\text{H}_{13}\text{N}_5^+$ ($[\text{M} + \text{H}]^+$) 300.1244.

(Z)-4-(Pyridin-2-yl(2-(pyridin-2-yl)hydrazineylidene)methyl)benzonitrile (10): isolated by flash chromatography on silica (SiO_2 , eluent: EtOAc); overall yield = 71%; yellow solid; (Z)-10 mp = 123–126 °C; ^1H NMR (600 MHz, CDCl_3) δ 12.93 (s, 1H), 8.78 (ddd, $J = 4.9$ Hz, 1.8 Hz, 0.9 Hz, 1H), 8.15 (ddd, $J = 4.9$ Hz, 1.8 Hz, 0.8 Hz, 1H), 7.74–7.71 (m, 1H), 7.68–7.61 (m, 4H), 7.59–7.54 (m, 1H), 7.41 (d, $J = 8.4$ Hz, 1H), 7.30 (ddd, $J = 7.6$ Hz, 4.9 Hz, 1.1 Hz, 1H), 7.24 (d, $J = 8.0$ Hz, 1H), 6.77 (ddd, $J = 7.2$ Hz, 4.9 Hz, 1.0 Hz, 1H) ppm; $^{13}\text{C}\{\text{H}\}$ NMR (151 MHz, CDCl_3) δ 156.7, 148.8, 148.0, 143.3, 138.1, 137.7, 137.8, 132.1, 129.2, 124.6, 123.4, 118.9, 116.8, 111.4, 107.7 ppm; IR $\tilde{\nu}_{\text{max}}$ 3100 (w), 2225 (m), 1586 (m), 1566 (m), 1491 (s), 1432 (s), 1301 (s) 1245 (m), 1134 (s), 848 (s), 792 (s), 729 (s), 592 (s) cm^{-1} ; HRMS (ESI) m/z for $\text{C}_{18}\text{H}_{13}\text{N}_5^+$ ($[\text{M} + \text{H}]^+$) found 300.1244, calcd $\text{C}_{18}\text{H}_{13}\text{N}_5^+$ ($[\text{M} + \text{H}]^+$) 300.1244.

(E)-2-(Naphthalen-1-yl(2-phenylhydrazineylidene)methyl)quinoline (11): isolated by flash chromatography on silica (SiO_2 , eluent = hexanes/EtOAc (5:1)); overall yield = 65% (260 mg); yellow solid; (E)-11 mp = 140–143 °C; ^1H NMR (300 MHz, DMSO- d_6) δ 9.19 (s, 1H), 8.56 (d, $J = 8.8$ Hz, 1H), 8.35 (d, $J = 8.8$ Hz, 1H), 8.07 (dd, $J = 12.5$ Hz, 8.3 Hz, 2H), 7.91 (d, $J = 8.2$ Hz, 1H), 7.70 (dd, $J = 8.1$ Hz, 7.1 Hz, 1H), 7.57–7.42 (m, 6H), 7.36 (ddd, $J = 8.2$ Hz, 6.6 Hz, 1.3 Hz, 1H), 7.31 (dd, $J = 8.7$ Hz, 1.2 Hz, 2H), 7.21 (dd, $J = 7.9$ Hz, 7.9 Hz, 2H), 6.81 (dd, $J = 7.2$ Hz, 7.2 Hz, 1H) ppm; $^{13}\text{C}\{\text{H}\}$ NMR (151 MHz, DMSO- d_6) δ 157.5, 147.4, 145.2, 142.4, 136.2, 134.1, 131.3, 131.2, 129.8, 129.4, 129.4, 129.2, 129.1, 128.6, 128.1, 127.4, 126.9, 126.6, 126.4, 125.4, 120.7, 118.9, 114.0 ppm; IR $\tilde{\nu}_{\text{max}}$ 3287 (w), 3069 (w), 1738 (w), 1598 (m), 1550 (s), 1504 (s), 1422 (s), 1308 (s), 1244 (s), 1147 (m), 836 (s), 788 (s), 754 (s), 697 (s) cm^{-1} ; HRMS (ESI) m/z for $\text{C}_{26}\text{H}_{19}\text{N}_3^+$ ($[\text{M} + \text{H}]^+$) found 374.1651, calcd $\text{C}_{26}\text{H}_{19}\text{N}_3^+$ ($[\text{M} + \text{H}]^+$) 374.1652.

(Z)-2-(Naphthalen-2-yl(2-phenylhydrazineylidene)methyl)quinoline (12): isolated by flash chromatography on silica (SiO_2 , eluent = hexanes/EtOAc (5:1)); overall yield = 70% (280 mg); yellow solid; (Z)-12 mp = 156–158 °C; ^1H NMR (300 MHz, CDCl_3) δ 12.71 (s, 1H), 8.50 (d, $J = 8.6$ Hz, 1H), 8.28 (d, $J = 8.4$ Hz, 1H), 8.07 (d, $J = 7.8$ Hz, 1H), 8.03–7.81 (m, 6H), 7.71 (dd, $J = 7.4$ Hz, 7.4 Hz, 1H), 7.58–7.44 (m, 4H), 7.31 (m, 4H), 6.87 (dd, $J = 7.0$ Hz, 7.0 Hz, 1H) ppm; $^{13}\text{C}\{\text{H}\}$ NMR (151 MHz, CDCl_3) δ 153.7, 147.1, 144.9, 144.9, 138.8, 138.0, 136.5, 133.3, 133.0, 130.8, 129.7, 129.4, 128.6, 128.4, 128.4, 128.0, 127.9, 127.5, 127.2, 126.9, 126.7, 126.1, 122.9, 120.9, 113.8 ppm; IR $\tilde{\nu}_{\text{max}}$ 3053 (w), 1744 (w), 1594 (w, m, C=N), 1497 (m), 1343 (s), 1343 (m), 1303 (m), 1232 (s), 1104 (m), 1068 (m), 872 (s), 830 (s), 796 (m), 759 (s), 688 (s); HRMS (ESI) m/z for $\text{C}_{26}\text{H}_{19}\text{N}_3^+$ ($[\text{M} + \text{H}]^+$) found 374.1652, calcd $\text{C}_{26}\text{H}_{19}\text{N}_3^+$ ($[\text{M} + \text{H}]^+$) 374.1652.

(Z)-2-(Naphthalen-2-yl(2-(pyridin-2-yl)hydrazineylidene)methyl)quinoline (13): isolated by flash chromatography on silica (SiO_2 , eluent = hexanes/EtOAc (3:1)); overall yield = 70% (280 mg); yellow solid; (Z)-13 mp = 145–148 °C; ^1H NMR (300 MHz, CDCl_3) δ 13.23 (s, 1H), 8.27 (d, $J = 8.4$ Hz, 1H), 8.14 (dd, $J = 9.6$ Hz, 7.1 Hz, 2H), 7.93–7.68 (m, 7H), 7.63–7.49 (m, 3H), 7.48–7.34 (m, 3H), 6.75 (dd, $J = 7.8$ Hz, 3.0 Hz, 1H) ppm; $^{13}\text{C}\{\text{H}\}$ NMR (151 MHz, CDCl_3) δ 157.3, 153.4, 148.1, 147.1, 140.2, 138.1, 137.0, 136.5, 133.4, 133.4, 130.5, 129.9, 128.5, 128.2, 127.9, 127.8, 127.7, 127.3, 126.6, 126.5, 122.8, 116.5, 108.1 ppm; IR $\tilde{\nu}_{\text{max}}$ 2912 (w), 1589 (m), 1492 (s), 1301 (m), 1137 (s), 1108 (s), 1085 (s), 826 (s), 770 (s),

726 (s), 657 (s) cm^{-1} ; HRMS (ESI) m/z for $\text{C}_{25}\text{H}_{18}\text{N}_4^+$ ($[\text{M} + \text{H}]^+$) found 375.1608, calcd $\text{C}_{25}\text{H}_{18}\text{N}_4^+$ ($[\text{M} + \text{H}]^+$) 375.1604.

■ ASSOCIATED CONTENT

SI Supporting Information

The following files are available free of charge. The Supporting Information is available free of charge at <https://pubs.acs.org/doi/10.1021/acs.joc.1c01174>.

Synthesis, NMR spectra, thermal kinetics study, and photochemical study (PDF)

Video S1 (MP4)

Video S2 (MP4)

Video S3 (MP4)

Archive containing XYZ coordinates of all calculated structures (ZIP)

FAIR data, including the primary NMR FID files, for compounds 1–21 (ZIP)

Accession Codes

CCDC 2070765 contains the supplementary crystallographic data for this paper. These data can be obtained free of charge via www.ccdc.cam.ac.uk/data_request/cif, or by emailing data_request@ccdc.cam.ac.uk, or by contacting The Cambridge Crystallographic Data Centre, 12 Union Road, Cambridge CB2 1EZ, UK; fax: +44 1223 336033.

■ AUTHOR INFORMATION

Corresponding Authors

Simon Budzák – Department of Chemistry, Faculty of Natural Sciences, Matej Bel University, 97400 Banská Bystrica, Slovakia; orcid.org/0000-0003-4811-8342; Email: simon.budzak@umb.sk

Marek Cigán – Department of Organic Chemistry, Faculty of Natural Sciences, Comenius University, 84215 Bratislava, Slovakia; orcid.org/0000-0001-7734-626X; Email: marek.cigan@uniba.sk

Authors

Bernard Mravec – Department of Organic Chemistry, Faculty of Natural Sciences, Comenius University, 84215 Bratislava, Slovakia

Miroslav Medved' – Department of Chemistry, Faculty of Natural Sciences, Matej Bel University, 97400 Banská Bystrica, Slovakia; Regional Centre of Advanced Technologies and Materials, Czech Advanced Technology and Research Institute (CATRIN), Palacký University Olomouc, 77900 Olomouc, Czech Republic

Lukáš F. Pašteka – Department of Physical and Theoretical Chemistry, Faculty of Natural Sciences, Comenius University, 84215 Bratislava, Slovakia; orcid.org/0000-0002-0617-0524

Chavdar Slavov – Institute of Physical and Theoretical Chemistry, Faculty of Biochemistry, Chemistry, Pharmacy, Goethe University, 60438 Frankfurt am Main, Germany

Torben Saßmannshausen – Institute of Physical and Theoretical Chemistry, Faculty of Biochemistry, Chemistry, Pharmacy, Goethe University, 60438 Frankfurt am Main, Germany

Josef Wachtveitl – Institute of Physical and Theoretical Chemistry, Faculty of Biochemistry, Chemistry, Pharmacy, Goethe University, 60438 Frankfurt am Main, Germany; orcid.org/0000-0002-8496-8240

Jozef Kožisek – Department of Physical Chemistry, Faculty of Chemical and Food Technology, Slovak University of Technology, 81237 Bratislava, Slovakia

Lea Hegedúsová – Department of Organic Chemistry, Faculty of Natural Sciences, Comenius University, 84215 Bratislava, Slovakia

Juraj Filo – Department of Organic Chemistry, Faculty of Natural Sciences, Comenius University, 84215 Bratislava, Slovakia; orcid.org/0000-0002-3995-2565

Complete contact information is available at: <https://pubs.acs.org/10.1021/acs.joc.1c01174>

Notes

The authors declare no competing financial interest.

■ ACKNOWLEDGMENTS

Financial support of the Slovak Research and Development Agency (APVV-20-0098 and APVV-19-0087) and the Scientific Grant Agency of the Slovak Republic (VEGA 1/0562/20, 1/0777/19, and 1/0718/19) is acknowledged. C.S. and J.W. acknowledge Deutsche Forschungsgemeinschaft (WA 1850/4-3). This project has received funding from the European Union's Horizon 2020 research and innovation program under grant agreement no. 810701 (LAMatCU). B.M., J.F., L.H., and M.C. acknowledge the support from the Operation Program of Integrated Infrastructure for the project: Advancing University Capacity and Competence in Research, Development and Innovation, ITMS2014+: 313021 × 329, cofinanced by the European Regional Development Fund. This research used resources of a High-Performance Computing Center of the Matej Bel University in Banská Bystrica using the HPC infrastructure acquired in projects ITMS 26230120002 and 26210120002 (Slovak infrastructure for high-performance computing) supported by the Research and Development Operational Program funded by the ERDF.

■ REFERENCES

- (1) Zhao, Y.; Ippolito, S.; Samorì, P. Functionalization of 2D Materials with Photosensitive Molecules: From Light-Responsive Hybrid Systems to Multifunctional Devices. *Adv. Opt. Mater.* **2019**, *7*, 1900286.
- (2) Qiu, H.; Zhao, Y.; Liu, Z.; Herder, M.; Hecht, S.; Samorì, P. Modulating the Charge Transport in 2D Semiconductors via Energy-Level Phototuning. *Adv. Mater.* **2019**, *31*, 1903402.
- (3) Mosciatti, T.; del Rosso, M. G.; Herder, M.; Frisch, J.; Koch, N.; Hecht, S.; Orgiu, E.; Samorì, P. Light-Modulation of the Charge Injection in a Polymer Thin-Film Transistor by Functionalizing the Electrodes with Bistable Photochromic Self-Assembled Monolayers. *Adv. Mater.* **2016**, *28*, 6606–6611.
- (4) Wang, Q.; Ligorio, G.; Diez-Cabanes, V.; Cornil, D.; Kobin, B.; Hildebrandt, J.; Nardi, M. V.; Timpel, M.; Hecht, S.; Cornil, J.; List-Kratochvil, E. J. W.; Koch, N. Dynamic Photoswitching of Electron Energy Levels at Hybrid ZnO/Organic Photochromic Molecule Junctions. *Adv. Funct. Mater.* **2018**, *28*, 1800716.
- (5) Wang, Q.; Diez-Cabanes, V.; Dell'Elce, S.; Liscio, A.; Kobin, B.; Li, H.; Brédas, J.-L.; Hecht, S.; Palermo, V.; List-Kratochvil, E. J. W.; Cornil, J.; Koch, N.; Ligorio, G. Dynamically Switching the Electronic and Electrostatic Properties of Indium–Tin Oxide Electrodes with Photochromic Monolayers: Toward Photoswitchable Optoelectronic Devices. *ACS Appl. Nano Mater.* **2019**, *2*, 1102–1110.
- (6) Morstein, J.; Trauner, D. New players in phototherapy: photopharmacology and bio-integrated optoelectronics. *Curr. Opin. Chem. Biol.* **2019**, *50*, 145–151.
- (7) Morstein, J.; Hill, R. Z.; Novak, A. J. E.; Feng, S.; Norman, D. D.; Donthamsetti, P. C.; Frank, J. A.; Harayama, T.; Williams, B. M.;

Parrill, A. L.; Tigyí, G. J.; Riezman, H.; Isacoff, E. Y.; Bautista, D. M.; Trauner, D. Optical control of sphingosine-1-phosphate formation and function. *Nat. Chem. Biol.* **2019**, *15*, 623–631.

(8) Velema, W. A.; Szymanski, W.; Feringa, B. L. Photopharmacology: Beyond Proof of Principle. *J. Am. Chem. Soc.* **2014**, *136*, 2178–2191.

(9) Broichhagen, J.; Frank, J. A.; Trauner, D. A Roadmap to Success in Photopharmacology. *Acc. Chem. Res.* **2015**, *48*, 1947–1960.

(10) Hauwert, N. J.; Mocking, T. A. M.; Pereira, D. D. C.; Koistra, A. J.; Wijnen, L. M.; Vreeker, G. C. M.; Verweij, E. W. E.; Boer, A. H. D.; Smit, M. J.; Graaf, C. D.; Vischer, H. F.; de Esch, I. J. P.; Wijtman, M.; Leurs, R. Synthesis and Characterization of a Bidirectional Photoswitchable Antagonist Toolbox for Real-Time GPCR Photopharmacology. *J. Am. Chem. Soc.* **2018**, *140*, 4232–4243.

(11) Broichhagen, J.; Podewin, T.; Meyer-Berg, H.; von Ohlen, Y.; Johnston, N. R.; Jones, B. J.; Bloom, S. R.; Rutter, G. A.; Hoffmann-Röder, A.; Hodson, D. J.; Trauner, D. Optical Control of Insulin Secretion Using an Incretin Switch. *Angew. Chem., Int. Ed.* **2015**, *54*, 15565–15569.

(12) Scheiner, M.; Sink, A.; Spatz, P.; Endres, E.; Decker, M. Photopharmacology on Acetylcholinesterase: Novel Photoswitchable Inhibitors with Improved Pharmacological Profiles. *ChemPhotoChem.* **2021**, *5*, 149–159.

(13) Hirayama, R.; Shiraki, A.; Naruse, M.; Nakamura, S.; Nakayama, H.; Kakue, T.; Shimobaba, T.; Ito, T. Optical Addressing of Multi-Colour Photochromic Material Mixture for Volumetric Display. *Sci. Rep.* **2016**, *6*, 31543.

(14) Guo, X.; Shao, B.; Zhou, S.; Aprahamian, I.; Chen, Z. Visualizing intracellular particles and precise control of drug release using an emissive hydrazone photochrome. *Chem. Sci.* **2020**, *11*, 3016–3021.

(15) Bléger, D.; Schwarz, J.; Brouwer, A. M.; Hecht, S. o-Fluoroazobenzenes as Readily Synthesized Photoswitches Offering Nearly Quantitative Two-Way Isomerization with Visible Light. *J. Am. Chem. Soc.* **2012**, *134*, 20597–20600.

(16) Weston, C. E.; Richardson, R. D.; Haycock, P. R.; White, A. J. P.; Fuchter, M. J. Arylazopyrazoles: Azoheteroarene Photoswitches Offering Quantitative Isomerization and Long Thermal Half-Lives. *J. Am. Chem. Soc.* **2014**, *136*, 11878–11881.

(17) Qian, H.; Pramanik, S.; Aprahamian, I. Photochromic Hydrazone Switches with Extremely Long Thermal Half-Lives. *J. Am. Chem. Soc.* **2017**, *139*, 9140–9143.

(18) Shao, B.; Qian, H.; Li, Q.; Aprahamian, I. Structure Property Analysis of the Solution and Solid-State Properties of Bistable Photochromic Hydrazones. *J. Am. Chem. Soc.* **2019**, *141*, 8364–8371.

(19) Tatum, L. A.; Su, X.; Aprahamian, I. Simple Hydrazone Building Blocks for Complicated Functional Materials. *Acc. Chem. Res.* **2014**, *47*, 2141–2149.

(20) Chaur, M. N.; Collado, D.; Lehn, J.-M. Configurational and Constitutional Information Storage: Multiple Dynamics in Systems Based on Pyridyl and Acyl Hydrazones. *Chem. - Eur. J.* **2011**, *17*, 248–258.

(21) Shao, B.; Aprahamian, I. Planarization-Induced Activation Wavelength Red-Shift and Thermal Half-Life Acceleration in Hydrazone Photoswitches. *ChemistryOpen* **2020**, *9*, 191–194.

(22) van Dijken, D. J.; Kovářček, P.; Ihrig, S. P.; Hecht, S. Acylhydrazones as Widely Tunable Photoswitches. *J. Am. Chem. Soc.* **2015**, *137*, 14982–14991.

(23) Lentès, P.; Frühwirt, P.; Freißmuth, H.; Moormann, W.; Kruse, F.; Gescheidt, G.; Herges, R. Photoswitching of Diazocines in Aqueous Media. *J. Org. Chem.* **2021**, *86*, 4355–4360.

(24) Siewertsen, R.; Neumann, H.; Buchheim-Stehn, B.; Herges, R.; Näther, C.; Renth, F.; Temps, F. Highly Efficient Reversible Z-E Photoisomerization of a Bridged Azobenzene with Visible Light through Resolved S1(nπ*) Absorption Bands. *J. Am. Chem. Soc.* **2009**, *131*, 15594–15595.

(25) Hammerich, M.; Schütt, C.; Stähler, C.; Lentès, P.; Röhricht, F.; Höppner, R.; Herges, R. Heterodiazocines: Synthesis and

Photochromic Properties, Trans to Cis Switching within the Bio-optical Window. *J. Am. Chem. Soc.* **2016**, *138*, 13111–13114.

(26) Lentès, P.; Stadler, E.; Röhricht, F.; Brahms, A.; Gröbner, J.; Sönnichsen, F. D.; Gescheidt, G.; Herges, R. Nitrogen Bridged Diazocines: Photochromes Switching within the Near-Infrared Region with High Quantum Yields in Organic Solvents and in Water. *J. Am. Chem. Soc.* **2019**, *141*, 13592–13600.

(27) Samanta, S.; Beharry, A. A.; Sadovski, O.; McCormick, T. M.; Babalhavaeji, A.; Tropepe, V.; Woolley, G. A. Photoswitching Azobenzene Compounds in Vivo with Red Light. *J. Am. Chem. Soc.* **2013**, *135*, 9777–9784.

(28) Dong, M.; Babalhavaeji, A.; Collins, C. V.; Jarrah, K.; Sadovski, O.; Dai, Q.; Woolley, G. A. Near-Infrared Photoswitching of Azobenzenes under Physiological Conditions. *J. Am. Chem. Soc.* **2017**, *139*, 13483–13486.

(29) Mravec, B.; Filo, J.; Csicsai, K.; Garaj, V.; Kemka, M.; Marini, A.; Mantero, M.; Bianco, A.; Cigán, M. Photoswitching hydrazones based on benzoylpyridine. *Phys. Chem. Chem. Phys.* **2019**, *21*, 24749–24757.

(30) Mravec, B.; Marini, A.; Tommasini, M.; Filo, J.; Cigán, M.; Mantero, M.; Tosi, S.; Canepa, M.; Bianco, A. Structural and Spectroscopic Properties of Benzoylpyridine-Based Hydrazones. *ChemPhysChem* **2021**, *22*, 533–541.

(31) Anslyn, E. V.; Dougherty, D. A. Experiments Related to Thermodynamics and Kinetics. In *Modern Physical Organic Chemistry*; University Science Books: Sausalito, 2004; pp 445–453.

(32) Hansch, C.; Leo, A.; Taft, R. W. A survey of Hammett substituent constants and resonance and field parameters. *Chem. Rev.* **1991**, *91*, 165–195.

(33) Reynolds, W. F.; Topsom, R. D. Field and resonance substituent constants for aromatic derivatives: limitations of Swain's revised F and R constants for predicting aromatic substituent effects. *J. Org. Chem.* **1984**, *49*, 1989–1992.

(34) Swain, C. G.; Unger, S. H.; Rosenquist, N. R.; Swain, M. S. Substituent effects on chemical reactivity. Improved evaluation of field and resonance components. *J. Am. Chem. Soc.* **1983**, *105*, 492–502.

(35) Chai, J.-D.; Head-Gordon, M. Long-range corrected hybrid density functionals with damped atom-atom dispersion corrections. *Phys. Chem. Chem. Phys.* **2008**, *10*, 6615–6620.

(36) Valeur, B.; Berberan-Santos, M. N. Effects of molecular structure on fluorescence. In *Molecular Fluorescence*; Wiley-VCH: Weinheim, 2012; pp 54–67.

(37) Mencaroni, L.; Carlotti, B.; Cesaretti, A.; Elisei, F.; Grgičević, A.; Škorić, I.; Spalletti, A. Competition between fluorescence and triplet production ruled by nitro groups in one-arm and two-arm styrylbenzene heteroanalogues. *Photochem. Photobiol. Sci.* **2020**, *19*, 1665–1676.

(38) Slavov, C.; Boumrifak, C.; Hammer, C. A.; Trojanowski, P.; Chen, X.; Lees, W. J.; Wachtveitl, J.; Braun, M. The ultrafast reactions in the photochromic cycle of water-soluble fulgimide photoswitches. *Phys. Chem. Chem. Phys.* **2016**, *18*, 10289–10296.

(39) Slavov, C.; Hartmann, H.; Wachtveitl, J. Implementation and Evaluation of Data Analysis Strategies for Time-Resolved Optical Spectroscopy. *Anal. Chem.* **2015**, *87*, 2328–2336.

(40) van Stokkum, I. H.; Larsen, D. S.; van Grondelle, R. Global and target analysis of time-resolved spectra. *Biochim. Biophys. Acta, Bioenerg.* **2004**, *1657*, 82–104.

(41) Iagatti, A.; Shao, B.; Credi, A.; Ventura, B.; Aprahamian, I.; Donato, M. D. Ultrafast processes triggered by one- and two-photon excitation of a photochromic and luminescent hydrazone. *Beilstein J. Org. Chem.* **2019**, *15*, 2438–2446.

(42) Wang, G.; Li, Y.; Song, T.; Shang, C.; Yang, J.; Lily, M.; Fang, Y.; Liu, F. Fluorescence Toggling Mechanism of Photochromic Phenylhydrazones: N–N Single Bond Rotation-Assisting E/Z Photoisomerization Differs from Imine. *J. Phys. Chem. A* **2020**, *124*, 6411–6419.

(43) Driscoll, E. W.; Hunt, J. R.; Dawlaty, J. M. Photobasicity in Quinolines: Origin and Tunability via the Substituents' Hammett Parameters. *J. Phys. Chem. Lett.* **2016**, *7*, 2093–2099.

- (44) Becke, A. D. A new mixing of Hartree–Fock and local density-functional theories. *J. Chem. Phys.* **1993**, *98*, 1372–1377.
- (45) Shao, Y.; Head-Gordon, M.; Krylov, A. I. The spin–flip approach within time-dependent density functional theory: Theory and applications to diradicals. *J. Chem. Phys.* **2003**, *118*, 4807–4818.